

**NASA  
Technical  
Paper  
2666**

November 1986

**Experimental Evaluation of Wall  
Mach Number Distributions of  
the Octagonal Test Section  
Proposed for NASA Lewis Research  
Center's Altitude Wind Tunnel**

**Douglas E. Harrington,  
Richard R. Burley,  
and Robert R. Corban**

(NASA-TP-2666) EXPERIMENTAL EVALUATION OF  
WALL MACH NUMBER DISTRIBUTIONS OF THE  
OCTAGONAL TEST SECTION PROPOSED FOR NASA  
LEWIS RESEARCH CENTER'S ALTITUDE WIND TUNNEL  
(NASA) 35 p

N87-17717

Unclassified  
CSCL 14B H1/09 43320

**NASA**

**NASA  
Technical  
Paper  
2666**

1986

**Experimental Evaluation of Wall  
Mach Number Distributions of  
the Octagonal Test Section  
Proposed for NASA Lewis Research  
Center's Altitude Wind Tunnel**

Douglas E. Harrington,  
Richard R. Burley,  
and Robert R. Corban

*Lewis Research Center  
Cleveland, Ohio*



National Aeronautics  
and Space Administration

Scientific and Technical  
Information Branch

## Summary

Wall Mach number distributions of the octagonal test section proposed for the NASA Lewis Research Center's Altitude Wind Tunnel (AWT) were experimentally determined over a range of free-stream Mach numbers from 0.2 to 0.92. The test section was slotted at the vertices of the octagon formed by its walls and had a nominal porosity of 11 percent. Reentry flaps were located at the test-section exit for the purpose of reingesting tunnel flow that had passed outside the test section through these slots. These flaps thus helped to maintain a uniform Mach number distribution in the test section. Flap angles were varied over a range of 0° (fully closed) to 9° (fully open). In addition, tunnel flow was bled through the test-section slots by means of a plenum evacuation system (PES) in order to maintain a uniform Mach number distribution in the test section. PES flow rates varied from 0 to 3 percent of tunnel flow. Test-section Reynolds number, based on the test-section equivalent diameter at the entrance, ranged from  $2.78 \times 10^6$  at a free-stream Mach number of 0.2 to  $9.16 \times 10^6$  at Mach 0.92.

Variations in reentry flap angle or PES flow rate had little or no effect on the Mach number distributions in the first 70 percent of the test section. However, in the aft region of the test section, flap angle and PES flow rate had a major impact on the Mach number distributions. Optimum PES flow rates were nominally 2 to 2.5 percent with the flaps fully closed and less than 1 percent when the flaps were fully open. The standard deviation of the test-section wall Mach numbers at the optimum PES flow rates was 0.003 or less. The tunnel flow accelerated from the nominal test-section entrance to the test-section midpoint for all free-stream Mach numbers except 0.2. The rate of acceleration increased with increasing free-stream Mach number. For example, at a free-stream Mach number of 0.4 the flow accelerated from a nominal wall Mach number of 0.399 at the entrance to 0.400 at the midpoint, an increase of 0.001. In contrast, at a free-stream Mach number of 0.92 the flow accelerated from Mach 0.913 to 0.92 over the same test-section distance, an increase of 0.007. Between the test-section midpoint and a point 70 percent into the test section, the flow stabilized and did not accelerate. Axial test-section Mach number distributions were independent of circumferential angular location.

## Introduction

It has been proposed that Lewis rehabilitate its Altitude Wind Tunnel (AWT) and extend its capabilities to meet the aeropropulsion needs of the next century. The AWT was first brought on line in 1944 and was used for aeropropulsion research until 1958, when it was converted into a series of altitude test chambers for space research. As currently configured (fig. 1), the AWT had a maximum free-stream Mach number of 0.6 at an altitude of 9144 m (30 000 ft) with total-temperature capability down to  $-38^{\circ}\text{C}$  ( $-36^{\circ}\text{F}$ ).

In addition to the expanded Mach number capability of 0.9+, the altitude pressure (up to 16 764 m (55 000 ft)) and low total-temperature capability (down to  $-51^{\circ}\text{C}$  ( $-60^{\circ}\text{F}$ )), the rehabilitated facility (fig. 2) would also have a number of other new capabilities. These include providing for an adverse weather test environment (icing, freezing rain, heavy rain, and snow) and acoustical measurements in the test section. The proposed test section would be octagonal in cross section with a 6.096-m (20-ft) span across the flats. The test-section walls would be acoustically treated, slotted, and surrounded by a 12.192-m-(40-ft-) diameter plenum tank that would be tied into a plenum evacuation system (PES) to provide for high-quality airflow with high-blockage models in the test section. The proposed rehabilitated AWT is described more completely in references 1 and 2.

Because of the magnitude of the AWT rehabilitation, the significant extensions to its original capability, and the lack of an adequate engineering base, it was determined that a modeling program (both experimental and analytical) was required to ensure the technical soundness of the new component designs. The experimental modeling effort comprised several 1/10-scale models. The 1/10-scale-model size was selected because of facility modeling experience at this scale (refs. 3 and 4), and because it represented the upper limit on size for which the exhaust flow capability available at Lewis could be used for providing model airflow. More detailed information regarding the AWT modeling program can be found in references 5 to 10.

This report presents the results of only one aspect of the AWT modeling effort: the experimentally determined Mach number distributions of the octagonal test section. These distributions were determined by modeling the high-speed leg

of the AWT, which is the section of the tunnel between corners 4 and 1 (fig. 2). The high-speed leg consisted of the tunnel settling chamber with flow-conditioning devices, the contraction, the slotted test section with the surrounding PES, and the high-speed diffuser. An engine exhaust scoop, planned for the full-scale AWT, was not installed for this phase of the test-section evaluation.

## Apparatus and Procedure

The facility, its instrumentation, and the test procedures are described completely in this section. All symbols are defined in appendix A.

### Facility Description

The test facility (figs. 3 and 4) is a 1/10-scale model of the high-speed leg proposed for the AWT. Dry air at atmospheric conditions was supplied by means of Lewis' central air supply system and entered the facility through a 76.2-cm- (30-in.-) diameter supply pipe. This pipe was connected to a 274.32-cm- (108-in.-) diameter plenum tank whose purpose was to prepare the air for entry into the settling chamber, contraction section, and test section of the tunnel. The supply pipe extended well into the plenum tank (fig. 5) and was perforated to allow the flow to distribute evenly in the plenum tank. To aid in turning the flow from vertical to horizontal, the pipe had a series of baffles attached at right angles to its centerline. To reduce the noise of the facility, the internal walls of the tank were acoustically treated with 15.24-cm- (6-in.-) thick compressed Kevlar. This reduced the internal diameter of the tank to 243.84 cm (96 in.). The plenum tank was 421.1 cm (165.8 in.) long. At the downstream end of the tank were four 34-mesh screens, each with a porosity of approximately 60 percent. The purpose of these screens was to reduce the turbulence as the flow left the tank and to provide relatively uniform flow to the settling chamber.

The plenum-tank total pressure was maintained at approximately 1 atmosphere; the total temperature was approximately room temperature (15 °C; 59 °F). Nominal mass flow rate ranged from approximately 21 kg/sec (46.3 lb/sec) at a test-section free-stream Mach number  $M_0$  of 0.2 to 66.5 kg/sec (146.6 lb/sec) at Mach 0.92.

Immediately downstream of the screens was a bellmouth that reduced the flow diameter to 155.45 cm (61.2 in.). A constant-area section 101.68 cm (40.03 in.) long followed immediately downstream of the bellmouth. This section comprised a 60.96-cm- (24.0-in.-) long spool section and a 40.72-cm- (16.03-in.-) long settling chamber. This settling chamber was a 1/10-scale model of the settling chamber proposed for the full-scale rehabilitated AWT. These sections were designed so that various flow-conditioning devices could be inserted into the airstream. Thus a number of combinations of screens, grids, and honeycomb flow straighteners could be tested. Several flow-straightener configurations were tested, but none

had any effect on the wall Mach number distributions observed in the test section nor on the results of this report.

Downstream of the settling chamber was a contraction section (figs. 6 and 7). The contraction served two purposes. The first was to accelerate the tunnel flow as efficiently as possible, with little or no separation, to the higher Mach numbers attained in the test section. The second was to make the transition from a circular cross-sectional flow area to an octagonal cross section with equal sides at the entrance to the test section. This transition occurred near the upstream portion of the contraction between  $X_{ts}/L_{ts} = -0.816$  and  $-0.667$ . The contraction was 155.45 cm (61.2 in.) in diameter at its upstream end ( $X_{ts}/L_{ts} = -0.867$ ) and had an area which was equivalent to a circle with a diameter of 60.96 cm (24 in.) at its downstream octagonal end ( $X_{ts}/L_{ts} = 0$ ), where it mated with the test section. Its nominal contraction ratio  $A_c/A_{ts}$  was 6.5, which is smaller than is usually desired to provide uniform flow to the test section. However, because of the existing structure of the full-scale AWT, geometric constraints, such as the contraction ratio, had to be imposed on the design of the high-speed leg of the rehabilitated AWT and, in turn, on its 1/10-scale model. The contraction was 145.374 cm (57.234 in.) long and had a ratio of length to maximum diameter of 0.935. Like the contraction ratio, the length of the contraction was a compromise based on constraints imposed by the existing structure of the AWT. Five small windows were located in the contraction walls (fig. 3) for observing the interior of the contraction and the entrance to the test section with television cameras. Except for these windows, this contraction was an exact 1/10-scale model of the full-scale contraction proposed for the rehabilitated AWT.

The octagonal, slotted test section (fig. 8) was 167.64 cm (66 in.) long. Longitudinal slots were located at the vertices of the octagon formed by the test-section walls. At the entrance to the test section the slots were closed. They opened linearly to their full width at a point 30.48 cm (12 in.) into the test section and continued at a constant width until they were 165.10 cm (65 in.) into the test section. At this point they opened linearly again for the last 2.54 cm (1.00 in.) of the test section. The width of the slots at the exit of the test section were equivalent to the width of the flaps at the entrance to the diffuser. Each test-section wall was comprised of several parts, a "flat" and two slot inserts that could be changed to vary test-section porosity (fig. 9). For this report the nominal test-section porosity at any axial location downstream of a point 30.48 cm (12 in.) into the test section was 11 percent based on the perimeter of a closed octagon. To account for boundary-layer growth on the contraction and tunnel walls, the test-section area was increased by diverging the walls located at circumferential angles of 45°, 135°, 225°, and 315° (i.e., walls 2, 4, 6, and 8). The top, bottom, and side walls (i.e., walls 1, 3, 5, and 7) did not diverge and were parallel to the test-section centerline.

The entrance to the test section ( $X_{ts}/L_{ts} = 0$ ) (fig. 10) was a closed octagon with eight equal sides and had an area

equivalent to that of a circle with a diameter of 60.96 cm (24 in.). The distance between walls was 59.355 cm (23.368 in.). The exit ( $X_{ts}/L_{ts} = 1.0$ ) (fig. 11) was an octagon with eight unequal sides and had an equivalent diameter of 61.288 cm (24.129 in.). The distance between the top and bottom walls, and side walls of the exit was the same as for the entrance, 59.355 cm (23.368 in.). However, the 45° walls (i.e., walls 2, 4, 6, and 8) diverged, and thus the distance between these walls was 60.005 cm (23.624 in.) as compared with 59.355 cm (23.368 in.) at the entrance. This difference represented an increase in the test-section cross-sectional area of approximately 1 percent to account for boundary-layer growth on the tunnel walls. The top, bottom, and side flats (fig. 12) were wider at the exit than at the entrance; the 45° flats were narrower at the exit than at the entrance. The slot inserts were identical for all of the flats, except that a right-hand and a left-hand set were required. The slot inserts were designed so that the slot opening was parallel to the vertex of the octagon. As with the contraction, the test section was an exact 1/10-scale model of the full-scale test section proposed for the rehabilitated AWT.

Following the test section was a diffuser (figs. 3 to 5). The diffuser was 182.78 cm (71.96 in.) long and comprised four major components: a flap section, an upstream transition section, and a downstream transition section (fig. 13) and a conical diffuser. The cross section of the entrance to the flap section ( $X_{ts}/L_{ts} = 1.0$ ) (fig. 14) was geometrically identical to the cross section of the exit to the test section ( $X_{ts}/L_{ts} = 1.0$ ) except for rectangular openings to permit the flaps to be located in an open position, thus allowing flow that had passed outside the test section through the test-section slots to be reingested into the main tunnel airstream. The flaps themselves were located at the end of each test-section slot. These flaps had the capability of being maintained in a fully closed position (0° with respect to the diffuser wall) or being positioned at any angle up to 9°. During this test program the flaps were tested at angles of 0°, 3°, 6°, and 9°. The nominal flap-section half angle was 3°. The purpose of the upstream transition section was to make the transition from a polygon with 16 unequal sides to one that had 16 equal sides. The purpose of the downstream transition section was to make the transition from 16 equal sides to a conical section. This conical section was geometrically similar to the existing full-scale AWT conical diffuser and differed in scale only. The conical diffuser half-angle was 3.5°.

The test section and parts of the contraction and diffuser were enclosed in the large PES tank (figs. 3 to 5). During tunnel operation air was exhausted from this tank and was used in conjunction with the reentry flaps to maintain a uniform Mach number distribution in the test section. This PES flow was exhausted through a 45.72-m- (18-in.-) diameter exhaust line to Lewis' altitude exhaust system. The exhaust line was located in the aft portion of the PES tank, which encompassed the flap and transition sections of the diffuser (figs. 4 and 5). The PES tank was to have been 121.92 cm (48.0 in.) in

diameter in the 1/10 scale. However, to provide adequate working space for installing instrumentation near the test section, the PES tank was fabricated with a diameter of 182.88 cm (72.0 in.) for the full length of the test section (fig. 5). To maintain the proper scale during testing, a foam filler material was used to reduce the diameter of the PES tank around the test section to 121.92 cm (48 in.).

## Instrumentation

Tunnel and PES mass flow rates were measured by means of standard ASME sharp-edged orifice plates. The tunnel orifice plate was located upstream of the test section; the PES plate was located downstream of the test section. Orifice temperatures were measured by copper-constantan (CuC) thermocouples; orifice pressures were measured by individual transducers. Tunnel flow rates ranged from approximately 21 kg/sec (46.3 lb/sec) at an  $M_0$  of 0.2 to 66.5 kg/sec (146.6 lb/sec) at an  $M_0$  of 0.92. PES flow rates ranged from 0 to 2.0 kg/sec (4.41 lb/sec). This corresponded to a ratio of PES flow to tunnel flow of 0 to 3 percent.

The total-pressure instrumentation at the contraction entrance was located at an axial location of  $X_{ts}/L_{ts} = -0.851$ , which was slightly downstream of the physical start of the contraction. This instrumentation (fig. 15) consisted of two rakes that spanned the entrance to the contraction section. Tunnel-wall static pressures were measured at various locations in the contraction and test sections. Three rows of 11 static-pressure taps each (fig. 16) were located in the contraction section at circumferential locations of 0°, 90°, and 270°. The contraction taps were essentially square-edged orifices and were 0.102 cm (0.040 in.) in diameter. Each test-section wall had 33 static-pressure taps (fig. 17). Each flat had 27 static-pressure taps equally spaced 6.35 cm (2.5 in.) apart on the centerline. In addition, each flat had two extra static-pressure taps at  $X_{ts}/L_{ts}$  of 0.045, 0.5, and 0.955. Thus the nominal entrance, middle, and exit of the test section each had 24 static-pressure taps. The test-section taps were 0.051 cm (0.020 in.) in diameter. All pressures other than orifice pressures were measured by using an electronically scanned pressure (ESP) system. This system consisted of a number of modules that contained 32 individual transducers each.

## Procedure

For each test run the flaps were manually set to one of the following angles—0°, 3°, 6°, or 9°. During a test run the test-section free-stream Mach number  $M_0$  was set to one of the following values—0.2, 0.4, 0.6, 0.8, or 0.92. Nominal  $M_0$  was set by using an average of the 24 wall static pressures measured halfway into the test section ( $X_{ts}/L_{ts} = 0.50$ ) in conjunction with the total pressure measured at the entrance to the contraction section ( $X_{ts}/L_{ts} = -0.851$ ). The Mach number set in this way was not influenced by either flap angle or PES flow rate. The defining equations for  $M_0$  and all other calculated Mach numbers are given in appendix B. At a given

$M_0$  and flap setting, PES flow was varied from 0 to 3 percent of tunnel flow in approximately 0.5-percent increments.

Test-section Reynolds number, based on the test-section equivalent diameter at the entrance, ranged from  $2.78 \times 10^6$  at an  $M_0$  of 0.2 to  $9.16 \times 10^6$  at an  $M_0$  of 0.92.

## Results and Discussion

### Mach Number Distributions

Selected test-section axial Mach number distributions were plotted for the complete range of test-section free-stream Mach numbers, flap angles, and PES flow rates tested (figs. 18 to 22). Distributions presented in these figures are along the centerline of each test-section flat. At each  $M_0$  data are shown for each of the four flap angles tested  $-0^\circ$ ,  $3^\circ$ ,  $6^\circ$ , and  $9^\circ$ . At each flap angle data are presented for little or no PES flow, a PES flow rate at or near the “optimum” flow rate, and a high PES flow rate (2.5 to 3.0 percent of tunnel flow). Qualitatively, the optimum PES flow rate corresponded to the PES flow that gave the flattest test-section wall Mach number  $M_w$  distribution for a particular flap angle and  $M_0$ . (A quantitative definition will be given later in figures 24 to 26.)

The Mach number distributions were independent of the test-section flat that they were measured on, or, in other words, they were independent of circumferential location. Typically the flow accelerated through the contraction and continued to accelerate to a Mach number slightly higher than  $M_0$ . However, the flow recompressed and stabilized at a Mach number at or slightly less than  $M_0$  once it had reached a point approximately 4.5 percent into the test section ( $X_{ts}/L_{ts} = 0.045$ ). The flow continued to mildly accelerate to a point approximately 50 percent into the test section. The Mach number then remained relatively constant to a point 70 percent into the test section. Variations in reentry flap angle or PES flow rate had little or no effect on the Mach number distributions upstream of this point. However, in the aft region of the test section ( $X_{ts}/L_{ts}$  nominally greater than 0.7), flap angle and PES flow rate had a major impact on the Mach number distributions. The flow generally accelerated or decelerated depending on the level of PES flow, flap angle, or both for a given  $M_0$ . With very little or no PES flow the main tunnel flow accelerated at the aft end of the test section. As the PES flow was gradually increased, the acceleration decreased until a point was reached when the Mach number distribution was the flattest. This point was then defined as the “optimum” PES flow rate for a given  $M_0$  and flap angle. Further increases in PES flow caused the tunnel flow to decelerate, corresponding to a diffusion related to the mass removal. Increasing flap angle had the same general effect on the aft test-section wall Mach number distributions as increasing PES flow rate.

At  $M_0 = 0.92$  certain combinations of PES flow and flap angle caused the test section to choke at its exit. Specifically,

for flap angles of  $0^\circ$ ,  $3^\circ$ , and  $6^\circ$  the flow choked when the nominal PES flow rates were relatively low. With the flaps set to  $0^\circ$  the flow choked with a nominal PES flow of 1 percent of tunnel flow (fig. 22(a)). Thus  $M_0$  of 0.92 or greater were not attainable with PES flow rates less than 1 percent and the flaps set to  $0^\circ$ . This problem was alleviated somewhat when the flaps were opened to  $3^\circ$ : the flow choked at a nominal flow rate of 0.5 percent (fig. 22(b)). At a flap angle of  $6^\circ$  the test section choked with no PES flow, indicating that to attain higher Mach numbers at this particular flap angle some PES flow would be required (fig. 22(c)). At  $9^\circ$  the problem was further alleviated when an  $M_0$  of 0.92 was achieved without any PES flow at all (fig. 22(d)). At  $9^\circ$  the exit did not actually choke but was very close to choking, indicating that slightly higher Mach numbers would be attainable without using any PES bleed flow.

Test-section circumferential wall Mach number distributions for the reentry flaps set at  $3^\circ$  (fig. 23) are representative of the trends exhibited for the other flap angles. Data were obtained at axial stations corresponding to the nominal test-section entrance ( $X_{ts}/L_{ts} = 0.045$ ), middle (0.5), and exit (0.955). Distributions in the forward ( $X_{ts}/L_{ts} = 0.273$ ) and the aft (0.727) portions of the test section are also included. As with the axial wall Mach number distributions data are presented for little or no PES flow, a PES flow rate at or near the “optimum” flow rate, and a high PES flow rate (2.5 to 3.0 percent of tunnel flow). The Mach number distributions in figure 23, as seen previously in figures 18 to 22, were completely independent of circumferential location. However, a localized trend in Mach number can be seen at the nominal test-section exit ( $X_{ts}/L_{ts} = 0.955$ ) with the PES flow at levels that were not optimum. Mach numbers on the centerline of each flat tended to be slightly higher than those measured off the centerline. The centerline data corresponded to the middle data point in each “cluster” of three data points.

### PES Flow Effects

As discussed previously, the qualitative definition of the “optimum” PES flow rate is the PES flow required to provide the flattest test-section wall Mach number  $M_w$  distribution for a particular flap angle and  $M_0$ . The next three figures quantify the definition of optimum PES flow rate.

As discussed in figures 18 to 22, variations in PES flow rate did not affect the Mach number distribution in the test section until a point nominally 70 percent into the test section had been reached. Thus one way to determine the flattest  $M_w$  distribution is to compare the wall Mach number calculated at the nominal test-section exit  $M_{ex}$  with the test-section free-stream Mach number  $M_0$ . By definition,  $M_0$  is synonymous with the wall Mach number calculated at the test-section midpoint and thus provides a basis for quantifying the optimum Mach number distribution. The general trend (fig. 24) was that  $M_{ex}/M_0$  decreased linearly with increasing levels of PES flow, indicating that the effect of bleeding flow through the

slots was to cause the flow to diffuse. A Mach number ratio of 1.0 (i.e.,  $M_{ex}/M_0 = 1.0$ ) indicated that the optimum level of PES flow had been attained. Nominal optimum PES flow rates ranged from 0.15 to 2.3 percent of tunnel flow depending on the flap angle and  $M_0$ .

Another approach to determining the optimum PES flow rates is based on the overall standard deviation of the individually measured test-section wall Mach numbers (fig. 25). The defining equations for this standard deviation and all other standard deviations calculated in this report are given in appendix B. The overall standard deviation of the test-section wall Mach numbers  $M_w$  was calculated by taking 248 of the 264 Mach numbers calculated on the test-section walls and using the arithmetic average  $\bar{M}_w$  of these Mach numbers as a reference. It does not include the Mach numbers calculated at a point just inside the test-section entrance ( $X_{ts}/L_{ts} = 0.008$ ) or those calculated at a point just inside the test-section exit ( $X_{ts}/L_{ts} = 0.992$ ). We felt that these regions of the test section were too close to the contraction and diffuser, respectively, and thus would unfairly penalize the test section for entrance and exit effects. In this approach to determining the optimum PES flow rates, the minimum standard deviation in  $M_w$  corresponded to the desired level of PES flow. At PES flow rates below optimum the standard deviation in  $M_w$  was high because the tunnel flow was accelerating through the aft end of the test section. At PES flow rates above optimum the standard deviation in wall  $M_w$  was high because the tunnel flow was diffusing through the aft end of the test section. As in figure 24 nominal optimum PES flow rates ranged from 0.15 to 2.3 percent of tunnel flow depending on the flap angle and the  $M_0$ . Note, however, that this method of determining the optimum PES flow rate was not as precise as the previous method because the minimum in the standard deviation often occurred over a range in PES flow rate. This made it difficult to precisely select the optimum PES flow rate. For example, at  $M_0 = 0.8$  and the flaps set to  $9^\circ$ , the optimum PES flow rate could be interpreted as being anywhere from 0.4 to 1.0 percent (fig. 25(d)). This figure also shows that the standard deviation of  $M_w$  at the optimum PES flow rates was 0.003 or less.

The two methods used to determine the optimum PES flow rates are compared over a range of  $M_0$  for the four flap angles tested in figure 26. The criterion for determining the optimum PES flow rate for the first method was to use figure 24 to determine when  $M_{ex}/M_0 = 1.0$ . The criterion for determining the optimum PES flow rate for the second method was to use figure 25 to determine the minimum standard deviation in  $M_w$  based on  $\bar{M}_w$ . The agreement between the two methods over a range of Mach numbers from 0.2 to 0.92 and flap angles from  $0^\circ$  to  $9^\circ$  was quite good. However, as noted previously, the first method was the more precise of the two. Optimum PES flow rates were nominally 2 to 2.5 percent when the flaps were fully closed ( $0^\circ$ ). Flow rates less than 1 percent were necessary when the flaps were fully open ( $9^\circ$ ).

## Flap Angle Effects

The effect of flap angle on the ratio of the Mach number at the test-section exit to the test-section free-stream Mach number ( $M_{ex}/M_0$ ) is presented in figure 27. Data are presented over a range of  $M_0$  from 0.2 to 0.92 and PES flow rates from 0 to 3 percent. Except at  $M_0 = 0.2$ , the general trend was that  $M_{ex}/M_0$  decreased linearly with increasing flap angle up to and including a flap angle of  $6^\circ$ . Further increase in flap angle to  $9^\circ$  did not affect  $M_{ex}/M_0$  as much as at the lower flap angles, indicating that higher flap angles would probably be less effective in influencing the flow characteristics in the aft portion of the test section. A Mach number ratio of 1.0 (i.e.,  $M_{ex}/M_0 = 1.0$ ) indicated that the "optimum" flap angle had been attained. Nominal optimum flap angles ranged from  $0^\circ$  to  $9^\circ$  depending on the PES flow rate and  $M_0$ . For no PES flow, flap angles greater than  $9^\circ$  appear to be required to obtain the optimum Mach number distribution through the test section. However, as stated earlier, higher flap angles may be less effective in optimizing the distributions.

Figure 28 summarizes the optimum flap angles as determined from figure 27 when the Mach number ratio  $M_{ex}/M_0$  was 1. When only 0.5 percent PES flow rate could be provided, optimum flap angles ranged from  $6^\circ$  to  $9^\circ$  depending on Mach number up to  $M_0 = 0.6$ . Flap angles less than  $2^\circ$  were required when PES flows of 2 percent could be provided. In all cases, for a given PES flow rate, higher flap angles were required as  $M_0$  was increased.

Figure 29 presents a tradeoff between flap angle and PES flow rate at the optimum levels. This figure was determined by combining the information provided in figures 26 and 28. As expected, increasing flap angle decreased the amount of PES flow required to maintain a flat Mach number distribution in the test section.

## Mach Number Effects

The effect of  $M_0$  on the overall standard deviation of the individually calculated  $M_w$  is presented in figure 30(a). Data are presented for the four flap angles tested ( $0^\circ$ ,  $3^\circ$ ,  $6^\circ$ , and  $9^\circ$ ) at the optimum levels of PES flow previously determined and discussed in figures 24 to 26. The standard deviation increased from approximately 0.001 at  $M_0 = 0.2$  to 0.003 at  $M_0 = 0.92$ . Generally, the standard deviation was not a function of flap angle.

To better understand the overall standard deviation of  $M_w$ , which was presented in figure 25 and 30(a) and was based on the average of 248 individually calculated Mach numbers, the standard deviation of  $M_w$  at five different axial locations was calculated (figs. 30(b) to (f)). Standard deviation of  $M_w$  is shown: at  $X_{ts}/L_{ts} = 0.045$ , 0.273, 0.500, 0.727, and 0.955. The reference Mach number at each axial location used to calculate standard deviation was an average of the individually calculated Mach numbers at that particular axial location (see appendix B). As with the previous figure, data are presented

for the four flap angles tested (0°, 3°, 6°, and 9°) at the optimum levels of PES flow. The standard deviation calculated in this manner was not a function of  $M_0$ . It was also quite low, generally less than 0.001 for all axial locations except the nominal test-section exit ( $X_{ts}/L_{ts} = 0.955$ ) where the standard deviation ranged from 0.001 to 0.002.

The ratio of test-section Mach number (as calculated at several different axial locations) to  $M_0$  is presented in figure 31 over the complete range of  $M_0$ , flap angles, and PES flows tested. In figure 31(a) the Mach number ratio  $M_{en}/M_0$  measured at the nominal test-section entrance ( $X_{ts}/L_{ts} = 0.045$ ) is shown as a function of  $M_0$ . As  $M_0$  increased, this ratio decreased from nominally 0.998 at  $M_0 = 0.2$  to 0.992 at  $M_0 = 0.92$ . However, this ratio was independent of variations in flap angle and PES flow rate, indicating that the entrance Mach number  $M_{en}$  was independent of flap angle and PES flow. Figure 31(b) presents the Mach number ratio  $M_{for}/M_0$  measured in the forward portion of the test section ( $X_{ts}/L_{ts} = 0.273$ ) as a function of  $M_0$ . As with the previous figure, when  $M_0$  was increased,  $M_{for}/M_0$  decreased. However, the Mach number ratio was generally higher, nominally 1.002 at  $M_0 = 0.2$  and decreasing to 0.996 at  $M_0 = 0.92$ —indicative of a modest acceleration from the test section entrance ( $X_{ts}/L_{ts} = 0.045$ ) to the forward portion of the test section ( $X_{ts}/L_{ts} = 0.273$ ). As with the entrance Mach number  $M_{en}$ , the forward Mach number  $M_{for}$  was independent of flap angle and PES flow. Figure 31(c) presents the ratio of the Mach number at the midpoint of the test section to the test-section free-stream Mach number  $M_{mp}/M_0$ . This ratio was 1.0 for all Mach numbers, flap angles, and PES flow rates because by definition  $M_{mp}$  and  $M_0$  were identical (fig. 31(c)). However, this figure does show that there was still a mild acceleration through the test section because  $M_{mp}/M_0$  was greater than  $M_{for}/M_0$  at all Mach numbers except  $M_0 = 0.2$ . Figure 31(d) presents the Mach number ratio  $M_{aft}/M_0$  measured in the aft portion of the test section ( $X_{ts}/L_{ts} = 0.727$ ) as a function of  $M_0$ . The Mach number ratio was nominally 1.0, indicating that the flow was no longer accelerating. However, the wider band in the  $M_{aft}/M_0$  data at this test-section axial location may indicate that the Mach number was now being slightly influenced by variations in flap angle and PES flow. At the nominal test-section exit ( $X_{ts}/L_{ts} = 0.955$ ) (fig. 31(e)) the flap angle and PES flow had a major impact on the test-section Mach number ratio  $M_{ex}/M_0$ .

Figure 32 summarizes the flow acceleration characteristics through the test section at various levels of  $M_0$ . This summary is based on the data presented in figures 31(a) to (d) and does not include data obtained at the nominal test-section exit ( $X_{ts}/L_{ts} = 0.955$ ), as presented in figure 31(e). Therefore, the Mach numbers in figure 32 are, for the most part, independent of flap angle and PES flow rate. The flow accelerated from the nominal test-section entrance ( $X_{ts}/L_{ts} = 0.045$ ) to the midpoint ( $X_{ts}/L_{ts} = 0.50$ ) for all  $M_0$  except 0.2. The rate of acceleration increased with increasing

$M_0$ . For example, at  $M_0 = 0.4$  the flow accelerated from a nominal Mach 0.399 at the test-section entrance to 0.400 at the test-section midpoint, an increase of 0.001. In contrast, at  $M_0 = 0.92$  the flow accelerated from Mach 0.913 to 0.920 over the same test-section distance, an increase of 0.007. Between the test-section midpoint and the aft portion of the test section ( $X_{ts}/L_{ts} = 0.727$ ), the flow stabilized and did not accelerate.

## Summary of Results

Wall Mach number distributions of the octagonal test section proposed for Lewis' Altitude Wind Tunnel were experimentally determined over a range of test-section free-stream Mach numbers  $M_0$  from 0.2 to 0.92. The test section was slotted at the vertices of the octagon formed by its walls and had a nominal porosity of 11 percent. Reentry flaps were located at the test-section exit for the purpose of reingesting tunnel flow that had passed outside the test section through these slots. These flaps thus helped to maintain a uniform Mach number distribution of the test section. Flap angles were varied over a range of 0° (fully closed) to 9° (fully open). In addition, tunnel flow was bled through the test-section slots by means of a plenum evacuation system (PES) to maintain a uniform Mach number distribution in the test section. PES flow rates varied from 0 to 3 percent of tunnel flow. Test-section Reynolds number, based on the test-section equivalent diameter at the entrance, ranged from  $2.78 \times 10^6$  at an  $M_0$  of 0.2 to  $9.16 \times 10^6$  at an  $M_0$  of 0.92. The following results were obtained:

1. Variations in reentry flap angle or PES flow rate had little or no effect on the Mach number distributions in the first 70 percent of the test section. However, in the aft region of the test section, flap angle and PES flow rate had a major impact on the Mach number distributions.
2. Optimum PES flow rates were nominally 2 to 2.5 percent with the flaps fully closed and less than 1 percent when the flaps were fully open.
3. The standard deviation of the test-section wall Mach numbers at the optimum PES flow rates was 0.003 or less.
4. Tunnel flow accelerated from the nominal test-section entrance to the test-section midpoint for all  $M_0$  except 0.2. The rate of acceleration increased with increasing  $M_0$ . For example, at an  $M_0$  of 0.4 the flow accelerated from a nominal Mach number of 0.399 at the entrance to 0.400 at the midpoint, an increase of 0.001. In contrast, at an  $M_0$  of 0.92 the flow accelerated from Mach 0.913 to 0.920 over the same test-section distance, an increase of 0.007. Between the midpoint and a point 70 percent into the test section, the flow stabilized and did not accelerate.
5. Axial test-section Mach number distributions were independent of circumferential angular location.

Lewis Research Center  
National Aeronautics and Space Administration  
Cleveland, Ohio, August 19, 1986

## Appendix A – Symbols

|             |  |
|-------------|--|
| $A_c$       | cross-sectional area at contraction entrance, $\text{cm}^2$<br>(in. $^2$ )   |
| $A_{ts}$    | cross-sectional area at test-section entrance, $\text{cm}^2$<br>(in. $^2$ )  |
| $L$         | length, cm (in.)   |
| $M$         | Mach number  |
| $M_w$       | individually calculated wall Mach number   |
| $\bar{M}_w$ | arithmetic average of 248 individually calculated test-section Mach numbers  |
| $N$         | number of static-pressure taps in test section used to calculate Mach number and standard deviation  |
| $P$         | static pressure, $\text{N}/\text{cm}^2$ ( $\text{lb}/\text{ft}^2$ )  |
| $P_{tc}$    | total pressure at entrance to contraction, $\text{N}/\text{cm}^2$ ( $\text{lb}/\text{in.}^2$ )   |
| $W_{pes}$   | plenum evacuation system mass flow rate as measured by orifice plate downstream of test section, $\text{kg}/\text{sec}$ ( $\text{lb}/\text{sec}$ ) |
| $W_{tun}$   | tunnel mass flow rate as measured by orifice plate upstream of facility, $\text{kg}/\text{sec}$ ( $\text{lb}/\text{sec}$ )                         |
| $X$         | axial location, cm (in.)   |
| $\alpha_f$  | flap angle relative to diffuser wall, deg  |
| $\theta$    | circumferential angular location (looking downstream), deg   |

|          |  |
|----------|--|
| $\sigma$ | standard deviation   |
| $\omega$ | ratio of plenum evacuation system mass flow rate to tunnel mass flow rate, $W_{pes}/W_{tun}$ , percent |

Subscripts:

|            |   |
|------------|---|
| <i>aft</i> | aft location in test section ( $X_{ts}/L_{ts} = 0.727$ )  |
| <i>c</i>   | contraction   |
| <i>en</i>  | nominal entrance to test section ( $X_{ts}/L_{ts} = 0.045$ )  |
| <i>ex</i>  | nominal exit of test section ( $X_{ts}/L_{ts} = 0.955$ )  |
| <i>fl</i>  | flap  |
| <i>for</i> | forward location in test section ( $X_{ts}/L_{ts} = 0.273$ )  |
| <i>mp</i>  | test-section midpoint ( $X_{ts}/L_{ts} = 0.50$ )  |
| <i>opt</i> | optimum   |
| <i>ref</i> | reference   |
| <i>ts</i>  | test section  |
| <i>w</i>   | wall  |
| <i>0</i>   | nominal test-section free-stream conditions as calculated at a point halfway into test section ( $X_{ts}/L_{ts} = 0.50$ ) |

## Appendix B – Calculations

The following equations define the Mach number and standard deviation, respectively, as calculated for this report:

$$M_{ref} = \left\{ 5.0 \left[ \left( P_{tc}/P_{ref} \right)^{2/7} - 1.0 \right] \right\}^{1/2}$$

$$\sigma_{ref} = \left\{ \frac{\sum_{i=1}^{N_{ref}} (M_i - M_{ref})^2}{N_{ref} - 1} \right\}^{1/2}$$

where  $ref$  is defined in the adjoining table:

| $ref$       | $X_{ts}/L_{ts}$ | $N_{ref}$ |
|-------------|-----------------|-----------|
| $w^a$       | -0.116 to 1.0   | 1         |
| $\bar{M}_w$ | ---             | 248       |
| <i>en</i>   | 0.045           | 24        |
| <i>for</i>  | .273            | 8         |
| <i>mp</i>   | .500            | 24        |
| <i>aft</i>  | .727            | 8         |
| <i>ex</i>   | .955            | 24        |
| 0           | .500            | 24        |

<sup>a</sup>Standard deviation is not defined for  $w$ .

and  $M_{ref}$  is an arithmetic average of the  $N_{ref}$  Mach numbers calculated at a given  $X_{ts}/L_{ts}$ .

## References

1. Chamberlin, R.: Altitude Wind Tunnel (AWT)-A Unique Facility for Propulsion System and Adverse Weather Testing. AIAA Paper 85-0314, Jan. 1985.
2. Blaha, B.J.; and Shaw, R.J.: The NASA Altitude Wind Tunnel: Its Role in Advanced Icing Research and Development. AIAA Paper 85-0090, Jan. 1985.
3. Corseglio, V.R.; Olson, L.E.; and Falarski, M.D.: Overview: Aerodynamic Features of the New 40x80/80x120 Foot Wind Tunnel Complex at NASA Ames Research Center. AIAA Paper 84-0601, Mar. 1984.
4. van Ditshuizen, J.C.A.: Design and Calibration of the 1/10th Scale Model of the NLR Low Speed Wind Tunnel LST 8x6. Wind Tunnel Design and Testing Techniques, AGARD CP-174, AGARD, Paris, France, 1976, pp. 8-1 to 8-15.
5. Abbott, J.M., et al.: Analytical and Physical Modeling Program for the NASA Lewis Research Center's Altitude Wind Tunnel (AWT). AIAA-85-0379, Jan. 1985.
6. Ciepluch, C.C., et al.: Progress in the Lewis Research Center Altitude Wind Tunnel (AWT) Modeling Program. 14th AIAA Aerodynamic Testing Conference, AIAA, 1986, pp. 183-192.
7. Gelder, T.F., et al.: Wind Tunnel Turning Vanes of Modern Design. AIAA-86-0044, Jan. 1986.
8. Towne, C.E., et al.: Analytical Modeling of Circuit Aerodynamics in the New NASA Lewis Altitude Wind Tunnel. AIAA Paper 85-0380, Jan. 1985.
9. Moore, R.D.; Boldman, D.R.; and Shyne, R.J.: Experimental Evaluation of Two Turning Vane Designs for High-Speed Corner of 0.1-Scale Model of NASA Lewis Research Center's Proposed Altitude Wind Tunnel. NASA TP-2570, 1986.
10. Boldman, D.R.; Moore, R.D.; and Shyne, R.J.: Experimental Evaluation of Two Turning Vane Designs for Fan Drive Corner of 0.1-Scaled Model of NASA Lewis Research Center's Proposed Altitude Wind Tunnel. NASA TP-2646, 1986.

ORIGINAL PAGE IS  
OF POOR QUALITY

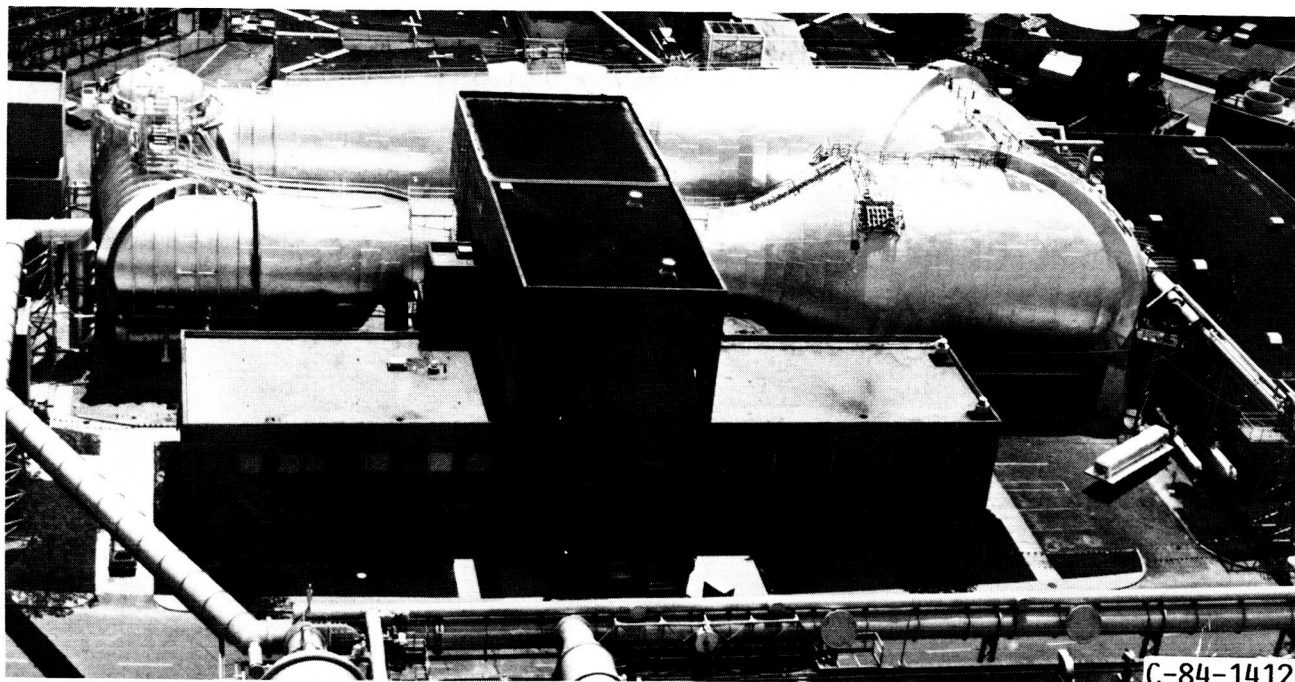


Figure 1.—Current configuration of Lewis Research Center's Altitude Wind Tunnel (AWT).

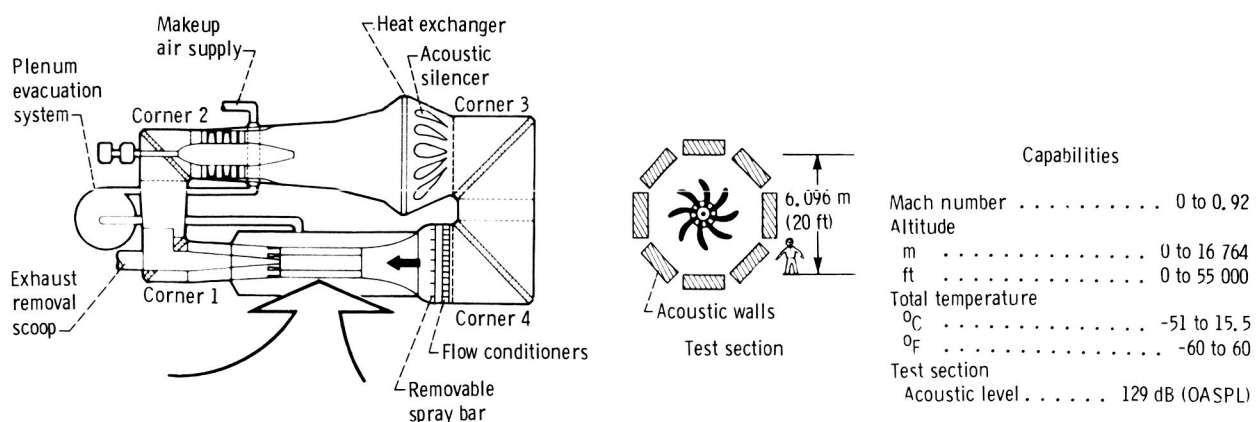


Figure 2.—Capabilities of modified and rehabilitated Altitude Wind Tunnel (AWT).

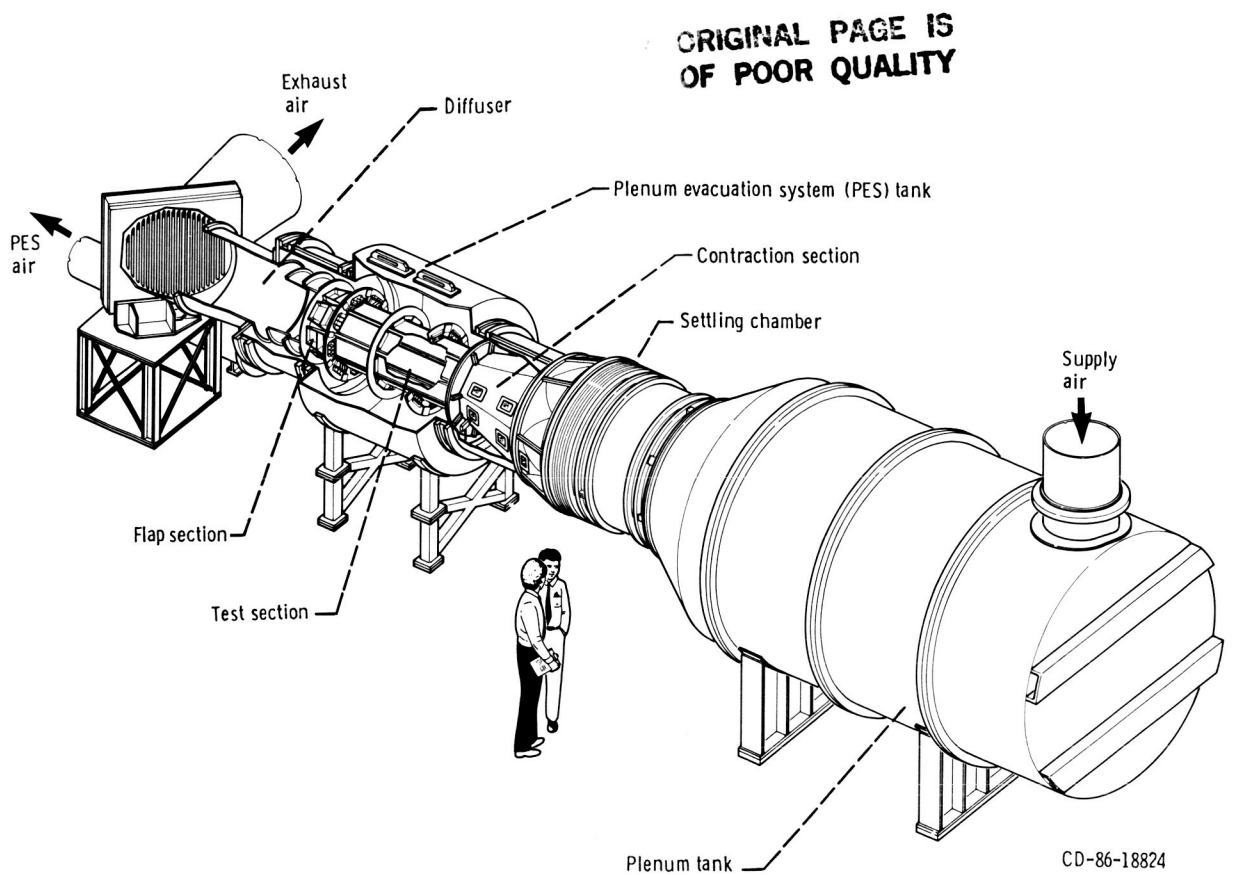


Figure 3.—Schematic of test facility.

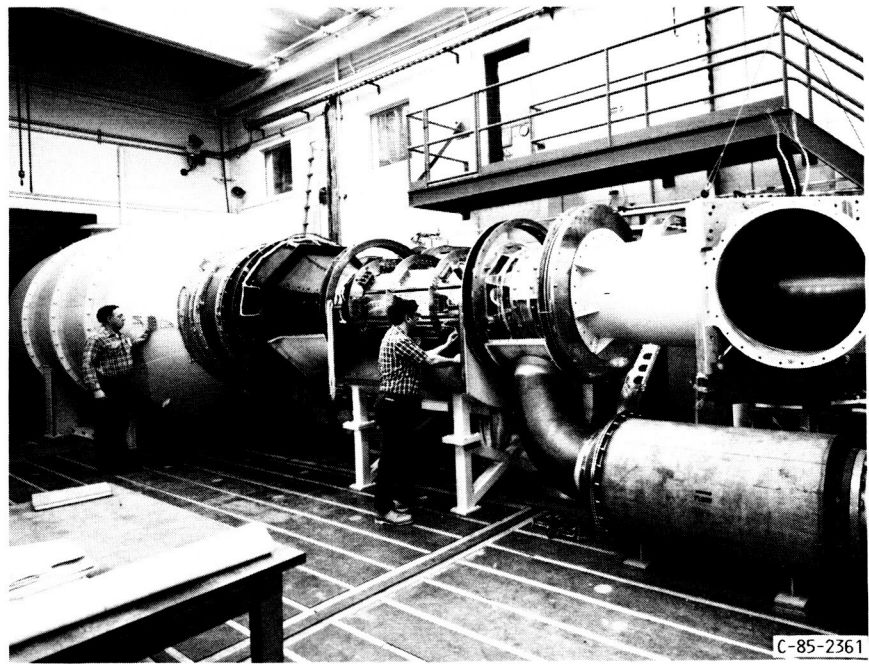


Figure 4.—Test facility (as seen from other side).

ORIGINAL PAGE IS  
OF POOR QUALITY

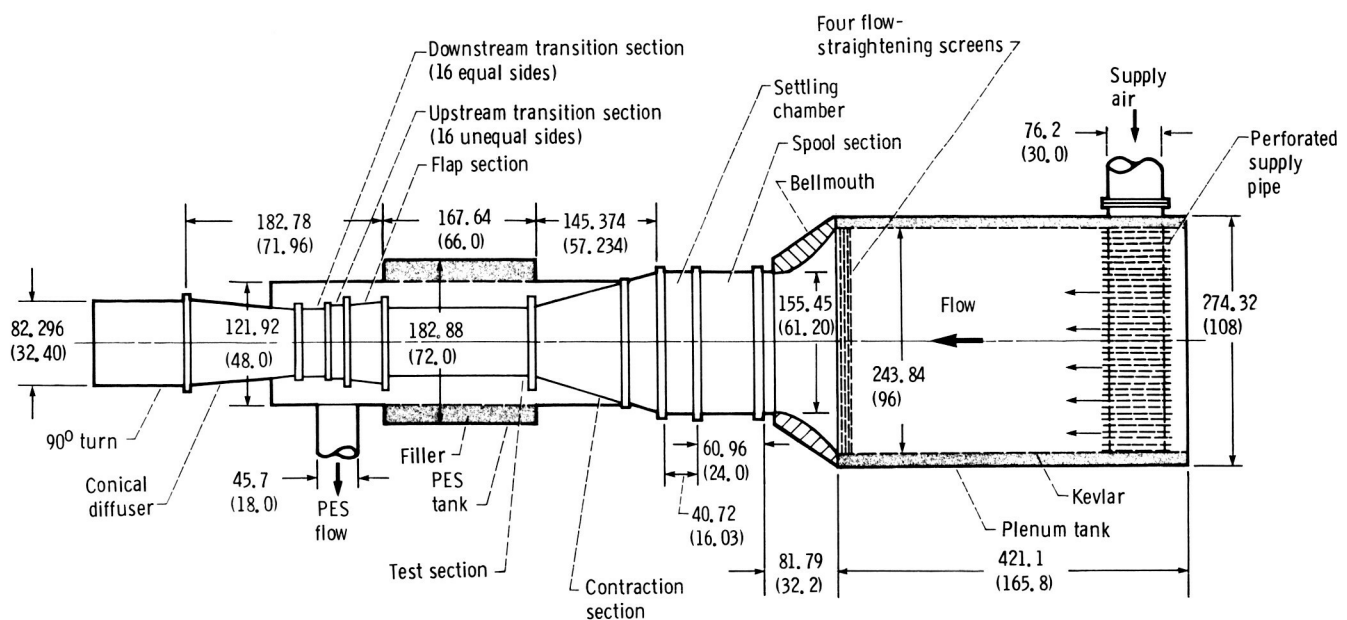


Figure 5.—Geometric details of facility (elevation). All dimensions are in centimeters (inches).

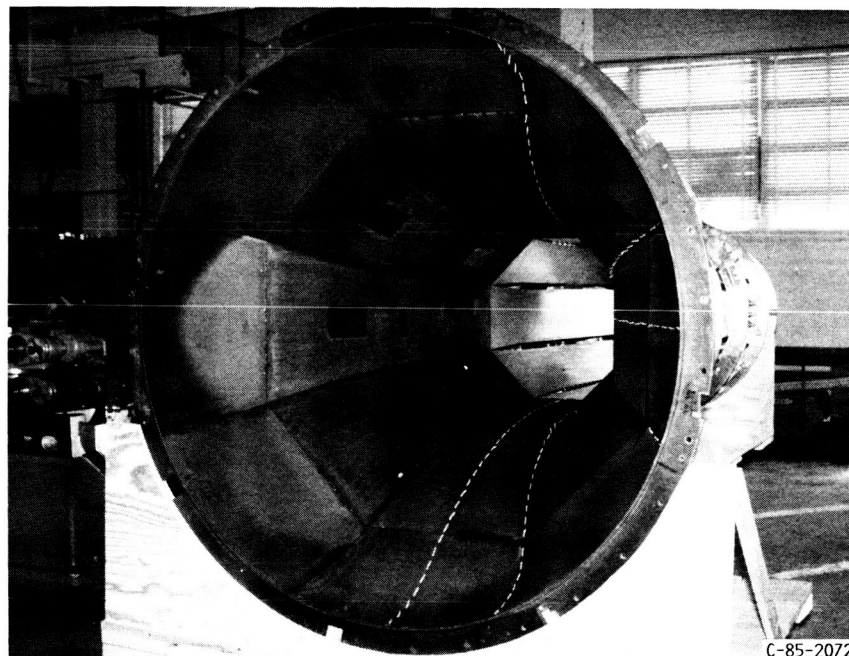


Figure 6.—Facility contraction section (looking downstream).

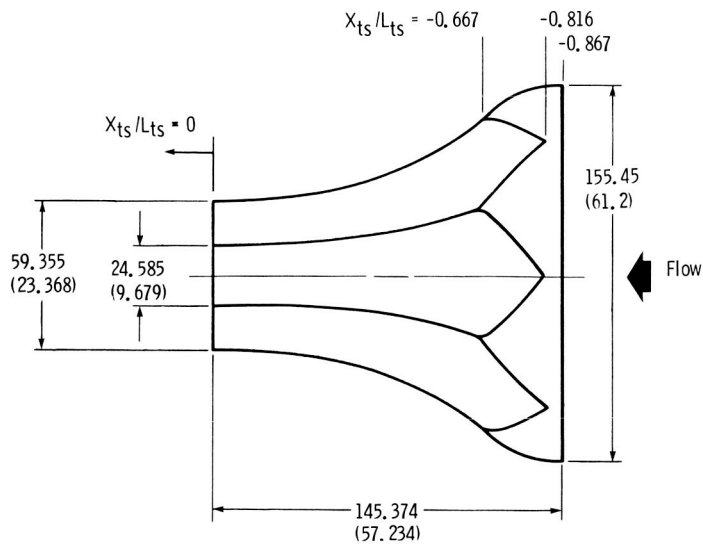


Figure 7.—Schematic of facility contraction. All dimensions are in centimeters (inches).

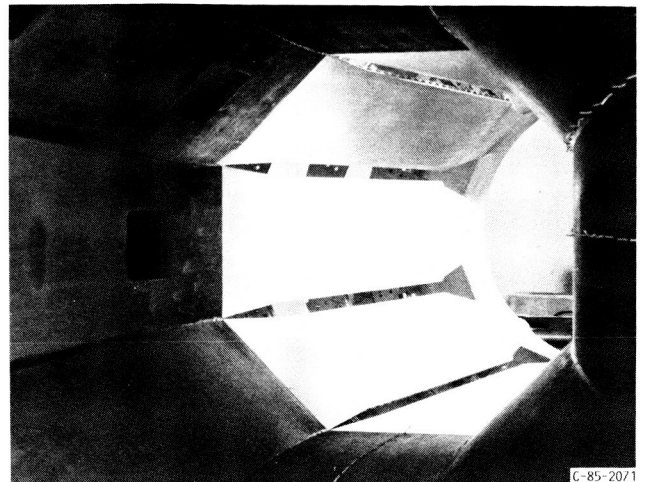


Figure 8.—Octagonal slotted test section (looking downstream from contraction section).

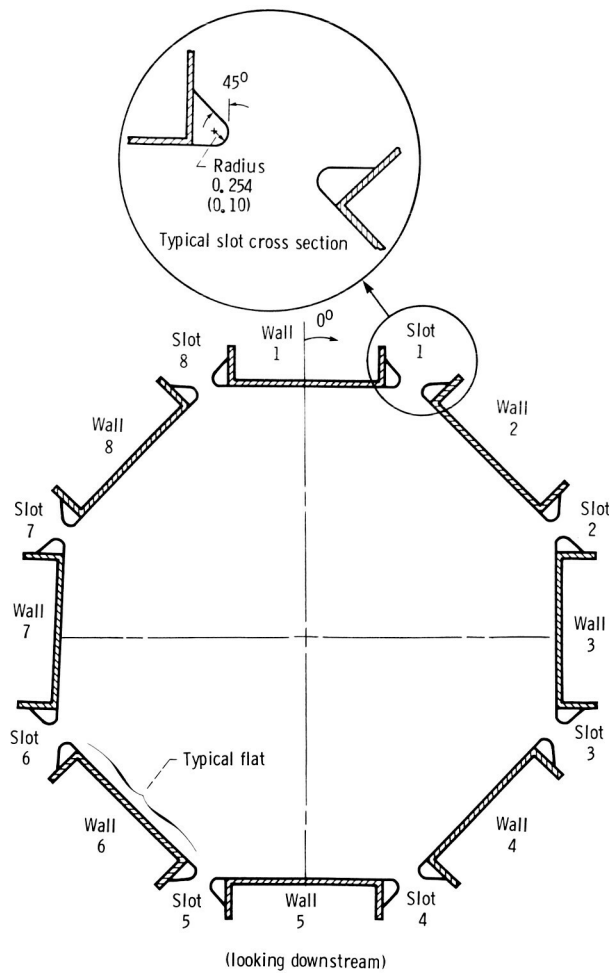


Figure 9.—Typical cross section of slotted, octagonal test section. All dimensions are in centimeters (inches).

ORIGINAL PAGE IS  
OF POOR QUALITY

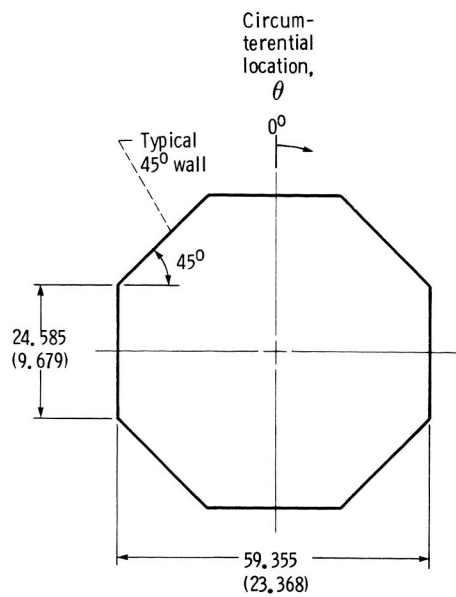
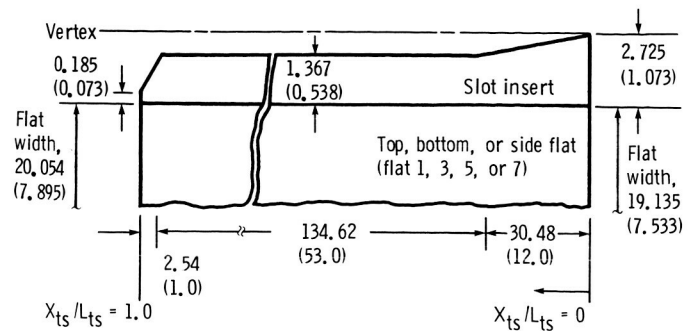
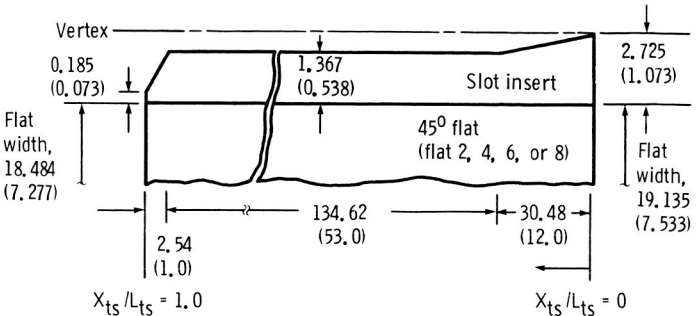


Figure 10.—Cross section of entrance to test section ( $X_{ts}/L_{ts} = 0$ ) (looking downstream). All dimensions are in centimeters (inches).



(a)



(b)

(a) Top, bottom, or side walls.  
 (b)  $45^\circ$  walls.

Figure 12.—Geometric details of test-section walls (half-planform). All dimensions are in centimeters (inches).

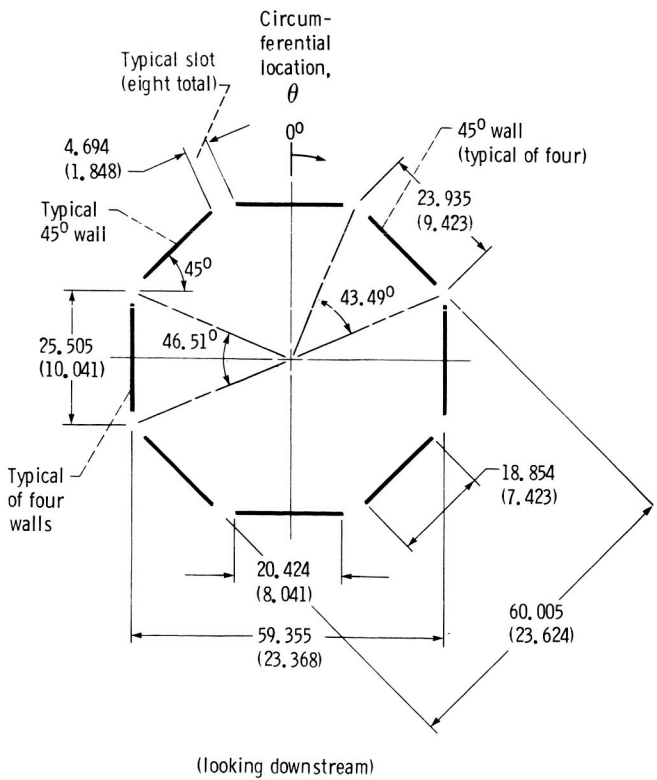


Figure 11.—Cross section of test-section exit ( $X_{ts}/L_{ts}$  = downstream). All dimensions are in centimeters (inches).

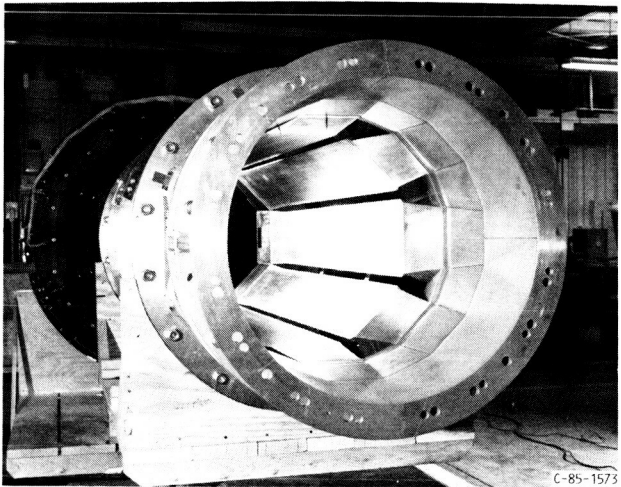
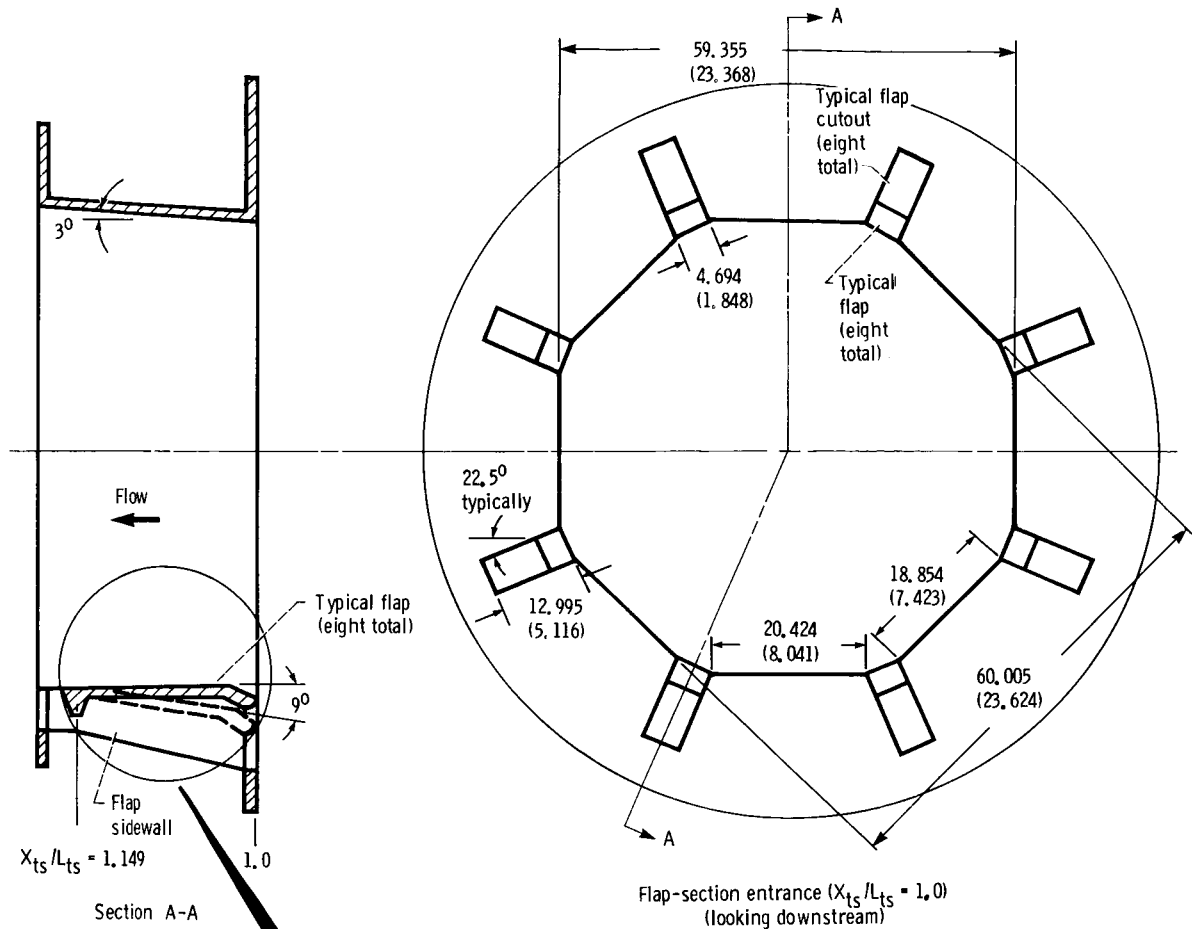


Figure 13.—Major components of diffuser including flap section and two transition sections (looking upstream into test section from conical diffuser).



| Flap leading-edge coordinates |       |          |       |
|-------------------------------|-------|----------|-------|
| $X_{fl}$                      |       | $Y_{fl}$ |       |
| cm                            | in.   | cm       | in.   |
| 0                             | 0     | 0        | 0     |
| .254                          | .100  | .711     | .280  |
| .508                          | .200  | .996     | .392  |
| .762                          | .300  | 1.207    | .475  |
| 1.016                         | .400  | 1.379    | .543  |
| 1.270                         | .500  | 1.524    | .600  |
| 1.524                         | .600  | 1.651    | .650  |
| 1.778                         | .700  | 1.763    | .694  |
| 2.032                         | .800  | 1.862    | .733  |
| 2.286                         | .900  | 1.951    | .768  |
| 2.540                         | 1.000 | 2.032    | .800  |
| 3.810                         | 1.500 | 2.327    | .916  |
| 5.080                         | 2.000 | 2.489    | .980  |
| 6.350                         | 2.500 | 2.540    | 1.000 |

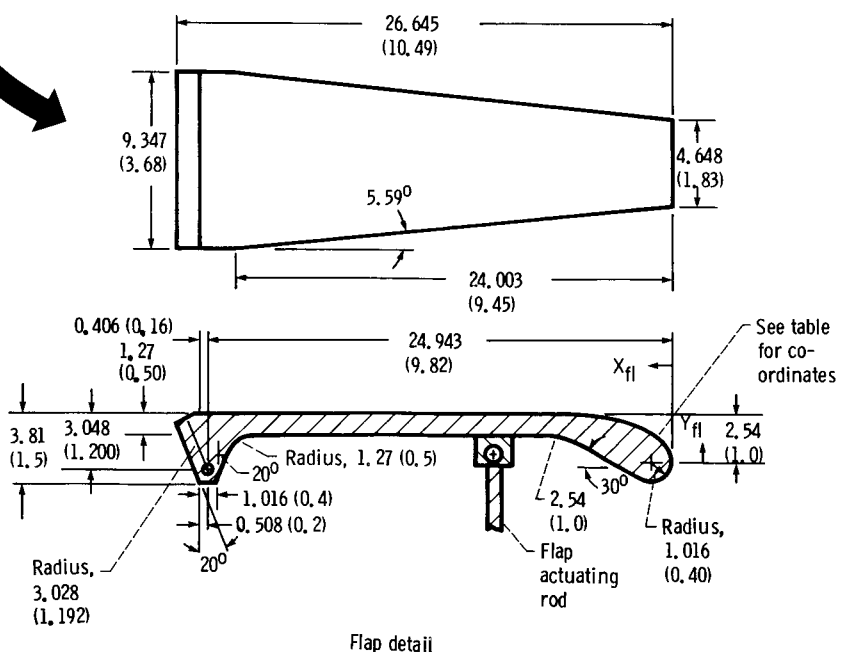


Figure 14.—Flap-section geometric details. All dimensions are in centimeters (inches).

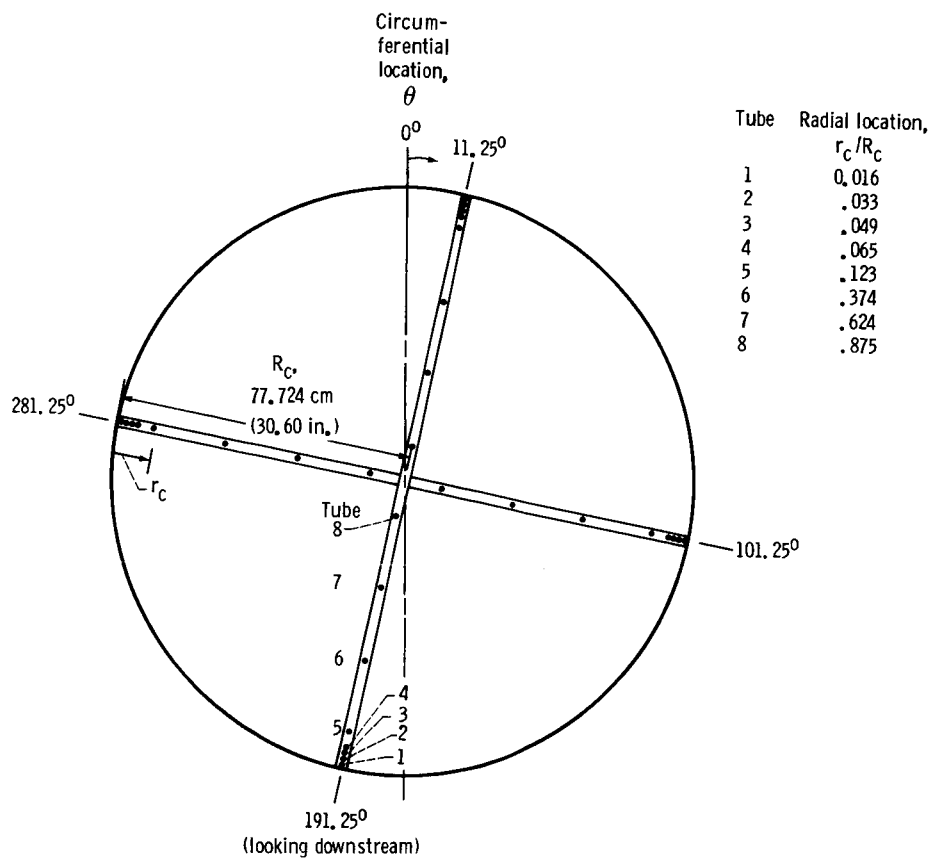


Figure 15.—Total-pressure instrumentation at nominal entrance to contraction section ( $X_{ts}/L_{ts} = -0.851$ ).

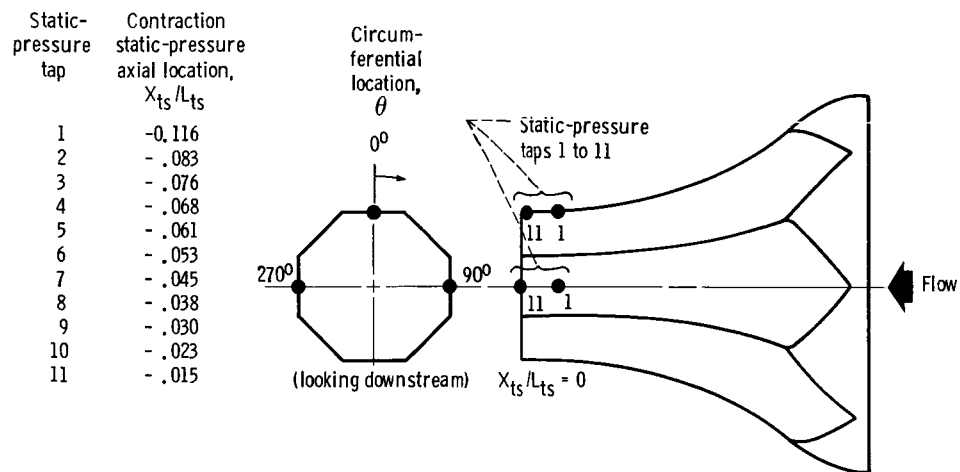
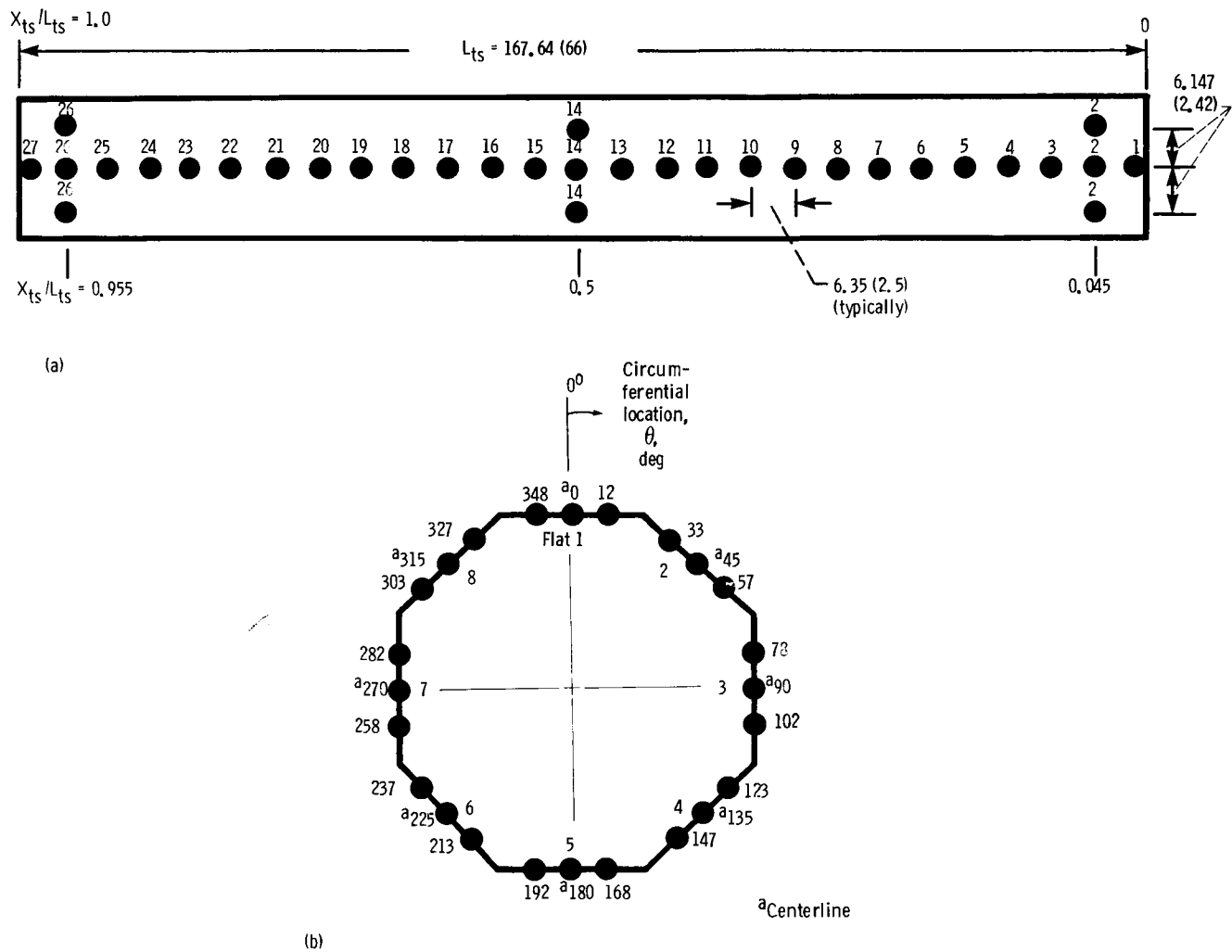


Figure 16.—Contraction static-pressure instrumentation.

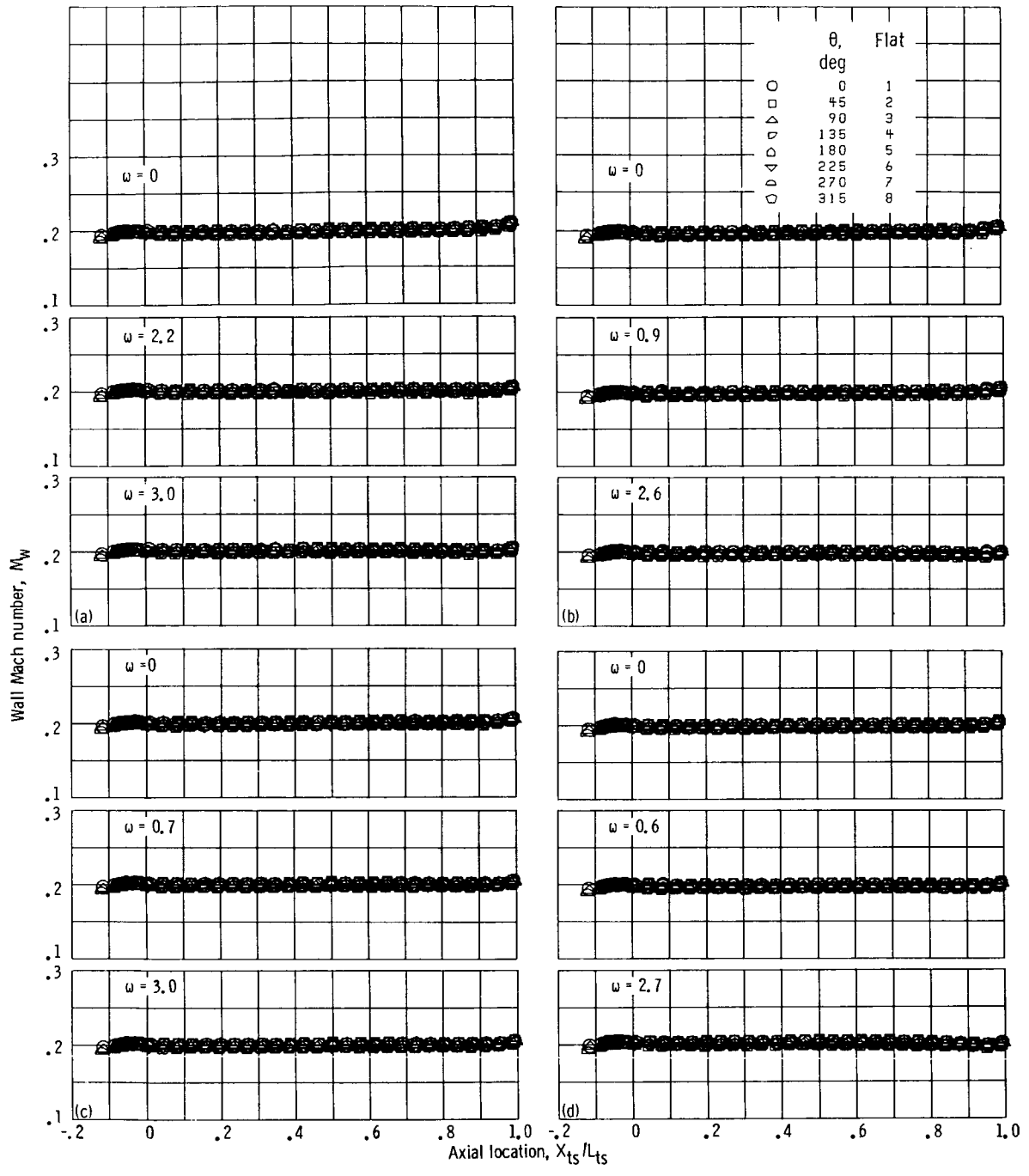
| Static-pressure tap number | Test-section static-pressure axial location, $X_{ts}/L_{ts}$ | Static-pressure tap number | Test-section static-pressure axial location, $X_{ts}/L_{ts}$ | Static-pressure tap number | Test-section static-pressure axial location, $X_{ts}/L_{ts}$ |
|----------------------------|--|----------------------------|--|----------------------------|--|
| 1                          | 0.008  | 10                         | 0.348  | 19                         | 0.689  |
| 2                          | .045   | 11                         | .386   | 20                         | .727   |
| 3                          | .083   | 12                         | .424   | 21                         | .765   |
| 4                          | .121   | 13                         | .462   | 22                         | .803   |
| 5                          | .159   | 14                         | .500   | 23                         | .841   |
| 6                          | .197   | 15                         | .538   | 24                         | .879   |
| 7                          | .235   | 16                         | .576   | 25                         | .917   |
| 8                          | .273   | 17                         | .614   | 26                         | .955   |
| 9                          | .311   | 18                         | .652   | 27                         | .992   |



(a) Flat 1 instrumentation (typical of all eight flats).

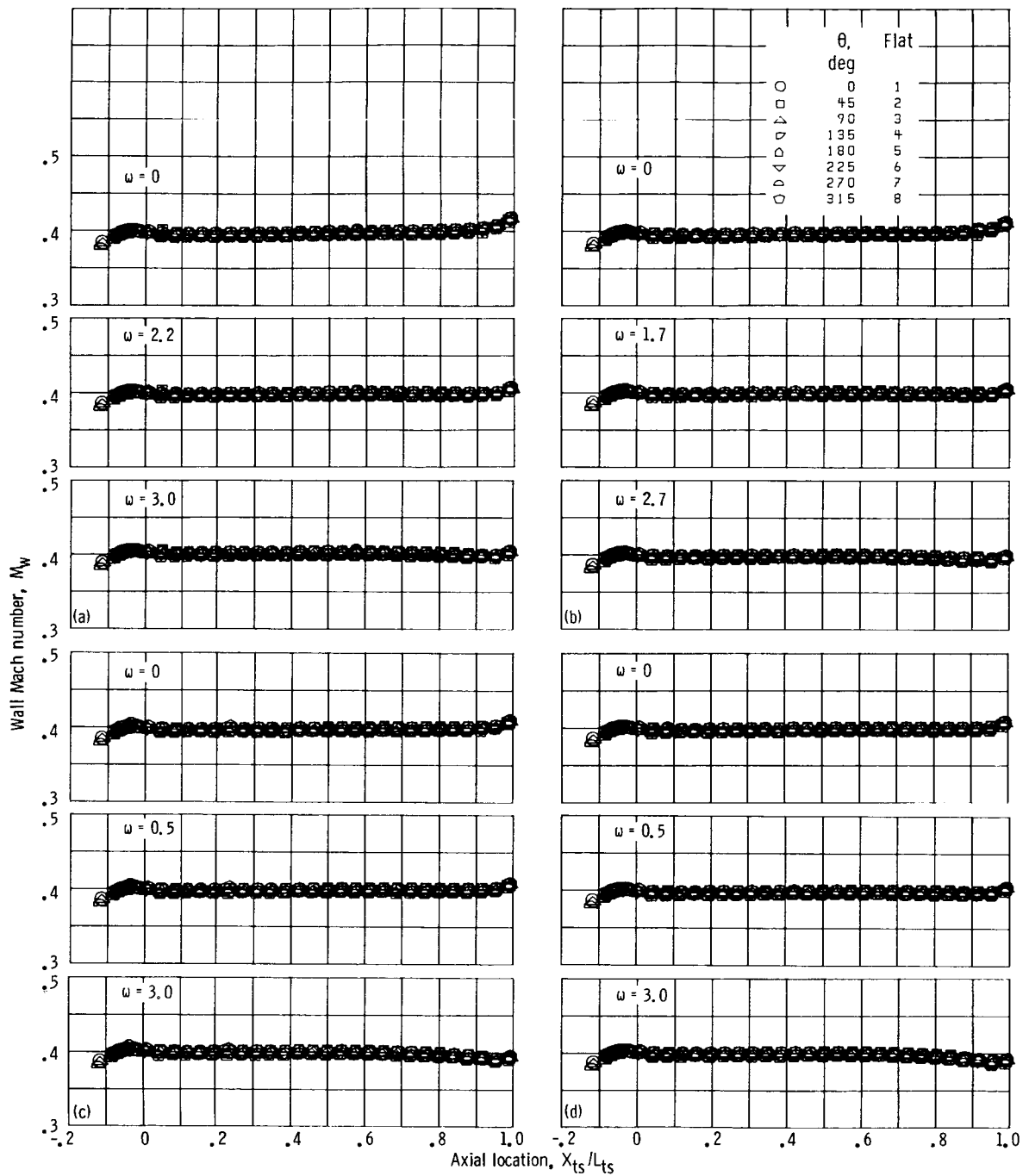
(b) Instrumentation at axial locations of  $X_{ts}/L_{ts} = 0.045, 0.5$ , and  $0.955$  (looking downstream).

Figure 17.—Test-section static-pressure instrumentation. All dimensions are in centimeters (inches).



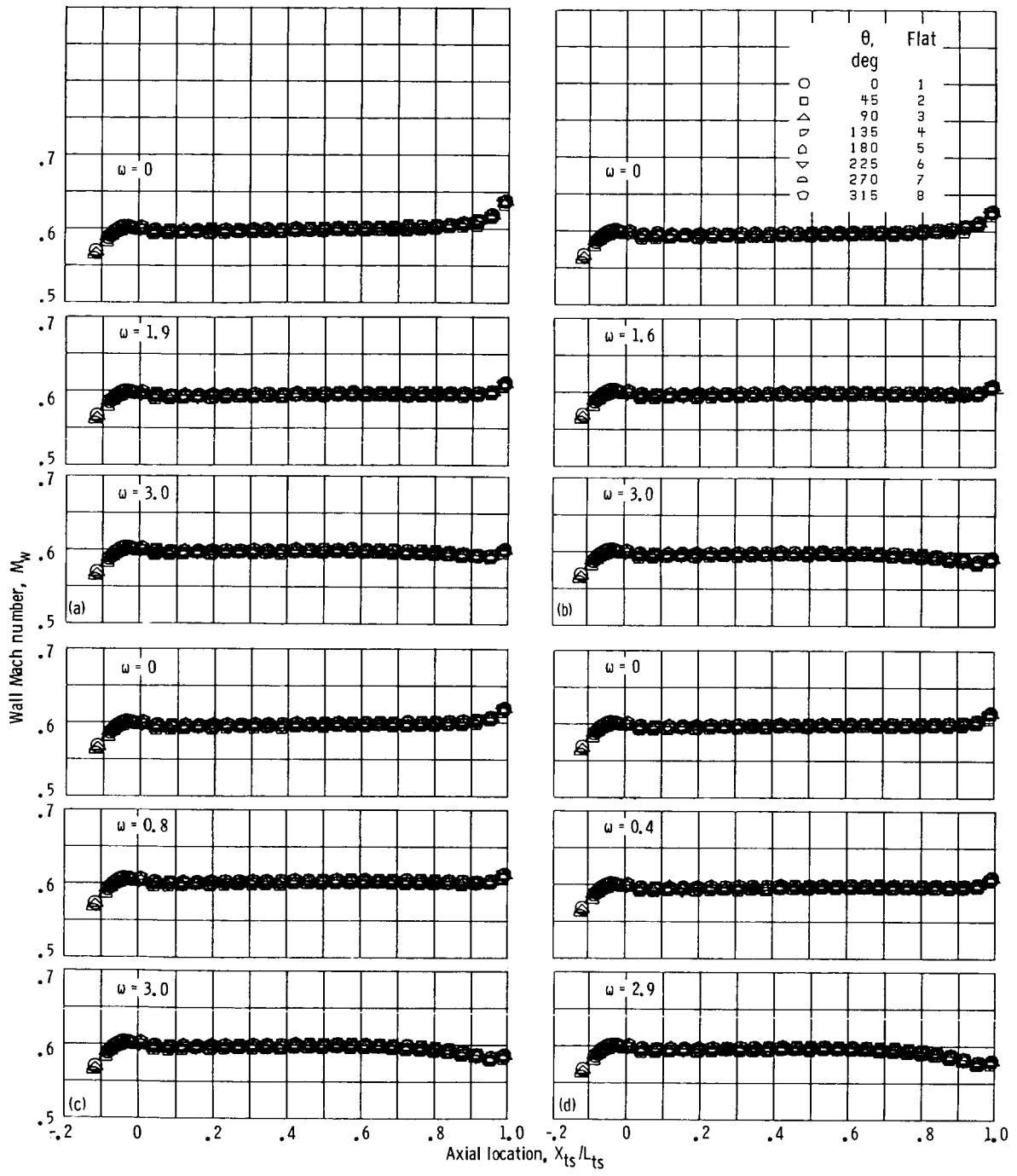
- (a) Flap angle, 0°.
- (b) Flap angle, 3°.
- (c) Flap angle, 6°.
- (d) Flap angle, 9°.

Figure 18.—Test-section wall axial Mach number  $M_w$  distributions for  $M_0 = 0.2$ . Flap angles, 0°, 3°, 6°, and 9°; PES flow rates  $\omega$ , 0 to 3 percent.



- (a) Flap angle, 0°.
- (b) Flap angle, 3°.
- (c) Flap angle, 6°.
- (d) Flap angle, 9°.

Figure 19.—Test-section wall axial Mach number  $M_w$  distributions for  $M_0 = 0.4$ . Flap angles, 0°, 3°, 6°, and 9°; PES flow rates  $\omega$ , 0 to 3 percent.



- (a) Flap angle,  $0^\circ$ .
- (b) Flap angle,  $3^\circ$ .
- (c) Flap angle,  $6^\circ$ .
- (d) Flap angle,  $9^\circ$ .

Figure 20.—Test-section wall axial Mach number  $M_w$  distributions for  $M_0 = 0.6$ . Flap angles,  $0^\circ$ ,  $3^\circ$ ,  $6^\circ$ , and  $9^\circ$ ; PES flow rates  $\omega$ , 0 to 3 percent.

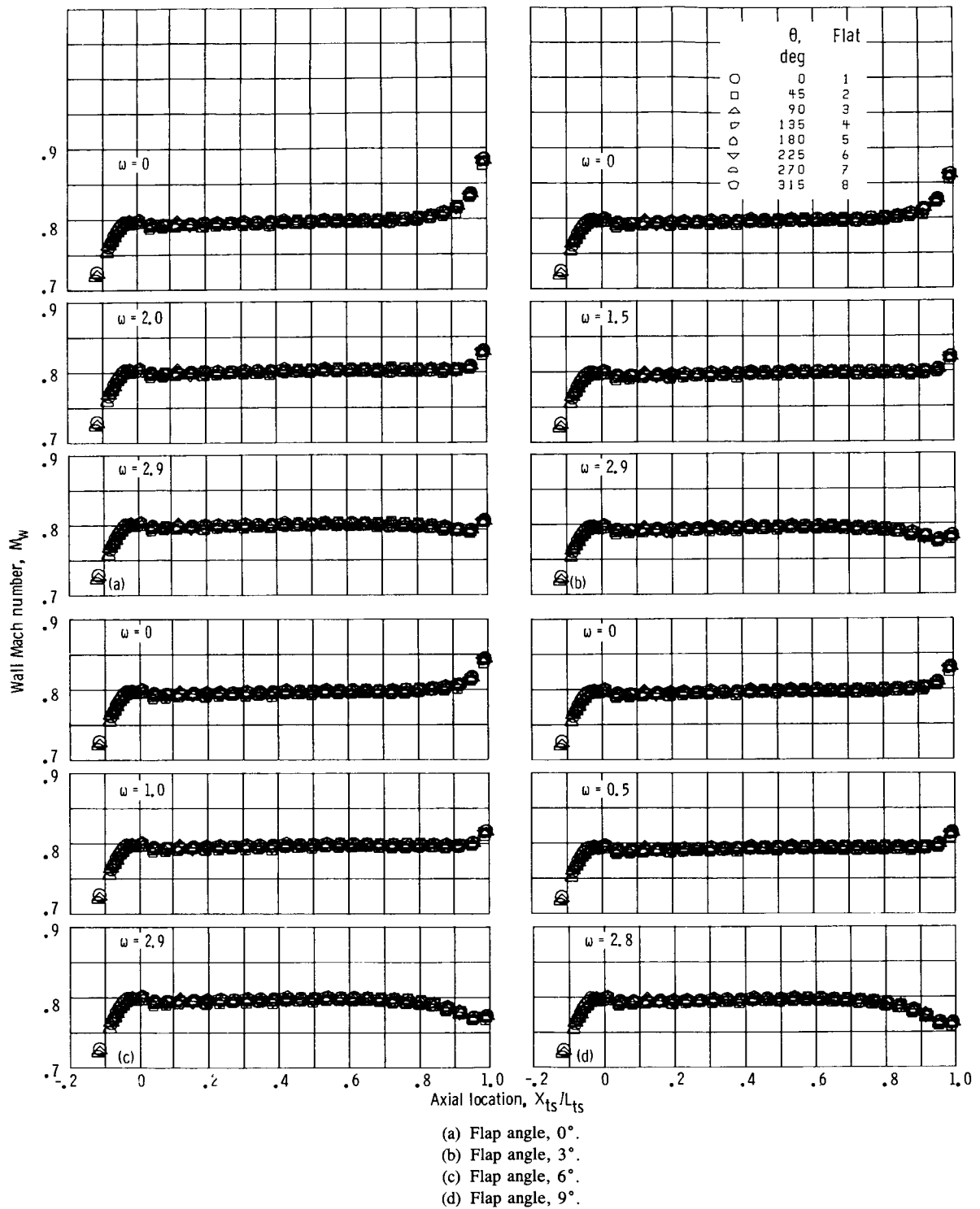


Figure 21.—Test-section wall axial Mach number  $M_w$  distributions for  $M_0 = 0.8$ . Flap angles,  $0^\circ$ ,  $3^\circ$ ,  $6^\circ$ , and  $9^\circ$ ; PES flow rates  $\omega$ , 0 to 3 percent.

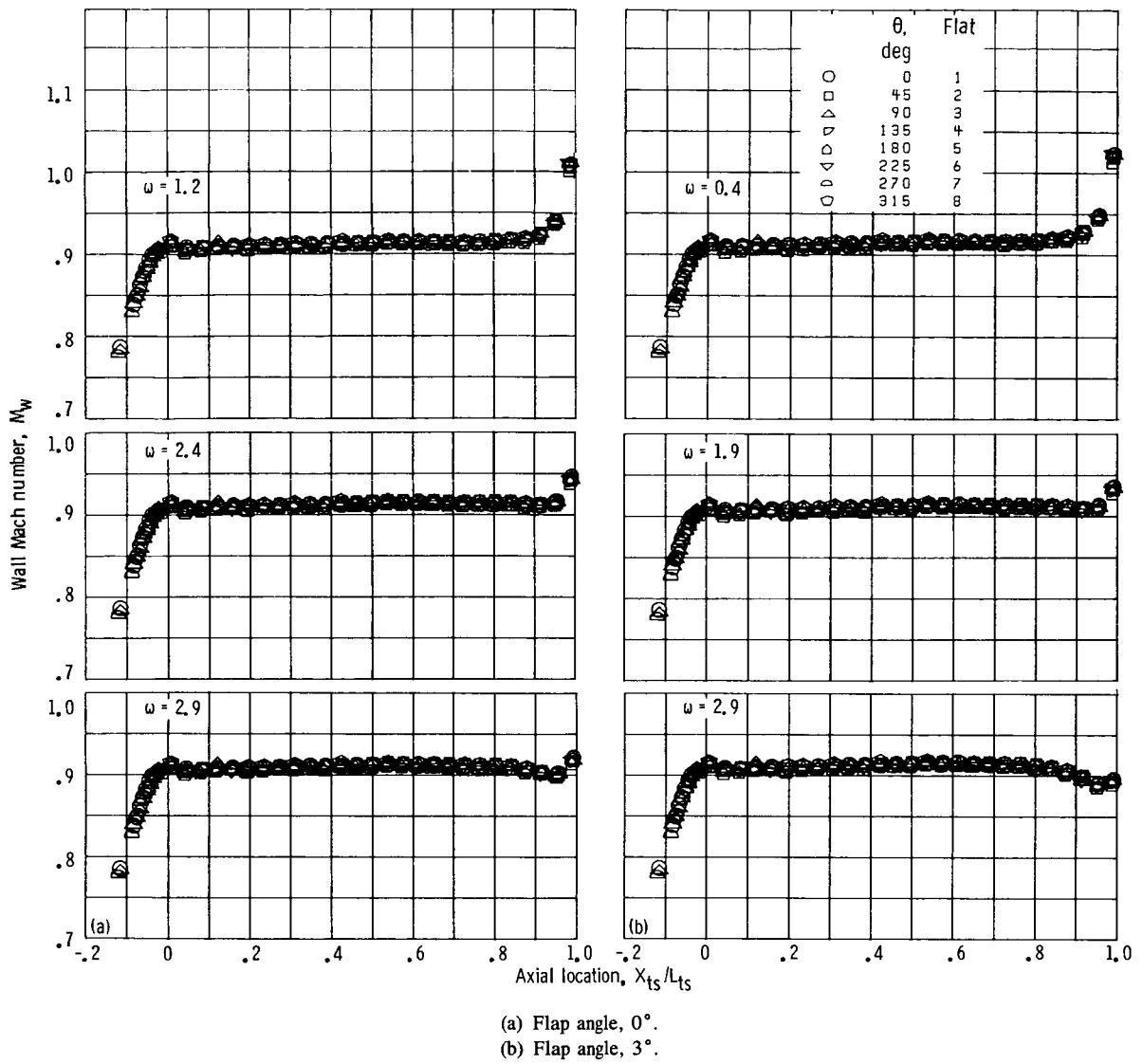
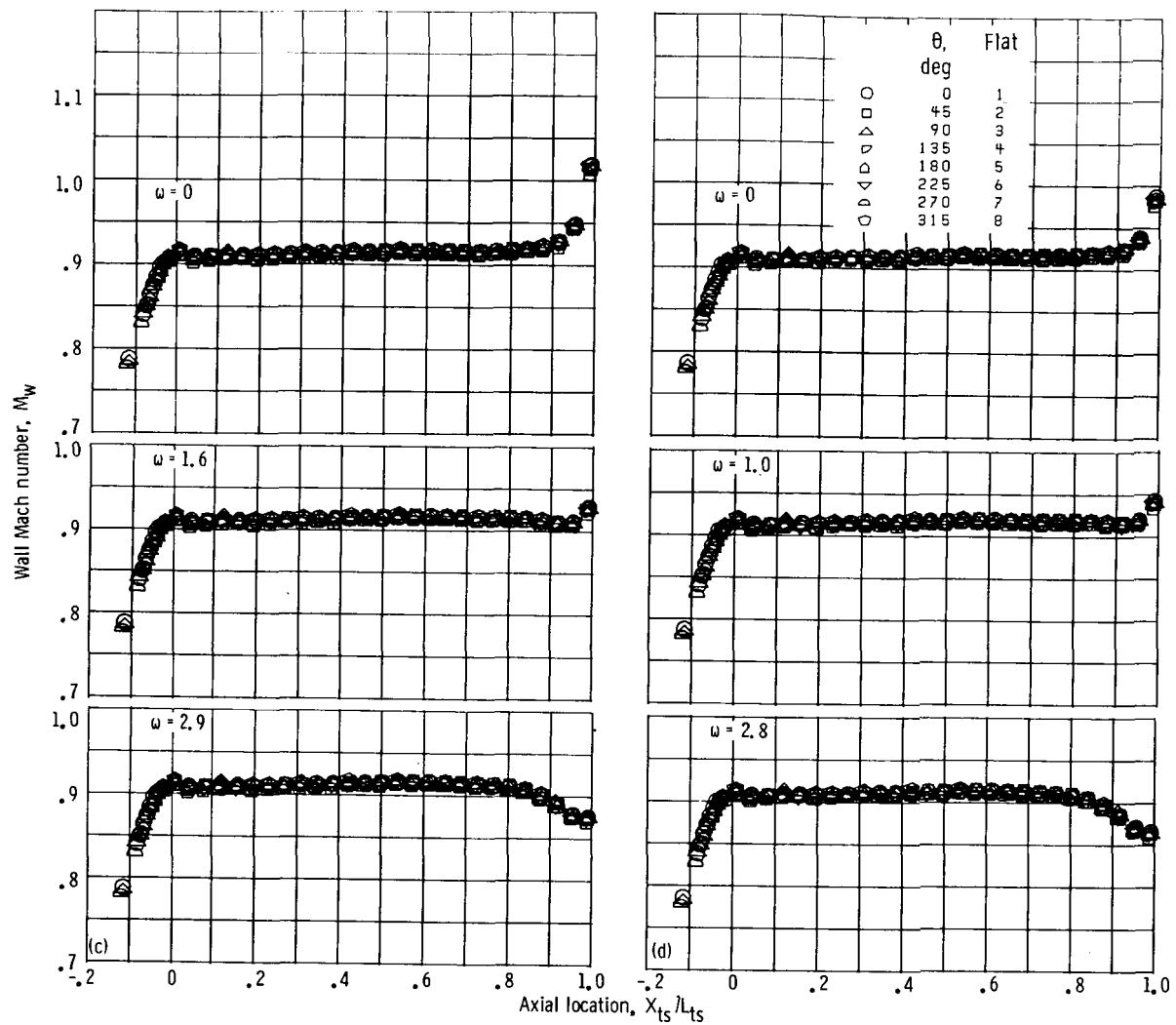


Figure 22.—Test-section wall axial Mach number  $M_w$  distributions for  $M_0 = 0.92$ . Flap angles,  $0^\circ$ ,  $3^\circ$ ,  $6^\circ$ , and  $9^\circ$ ; PES flow rates  $\omega$ , 0 to 3 percent.



(c) Flap angle,  $6^\circ$ .

(d) Flap angle,  $9^\circ$ .

Figure 22.—Concluded.

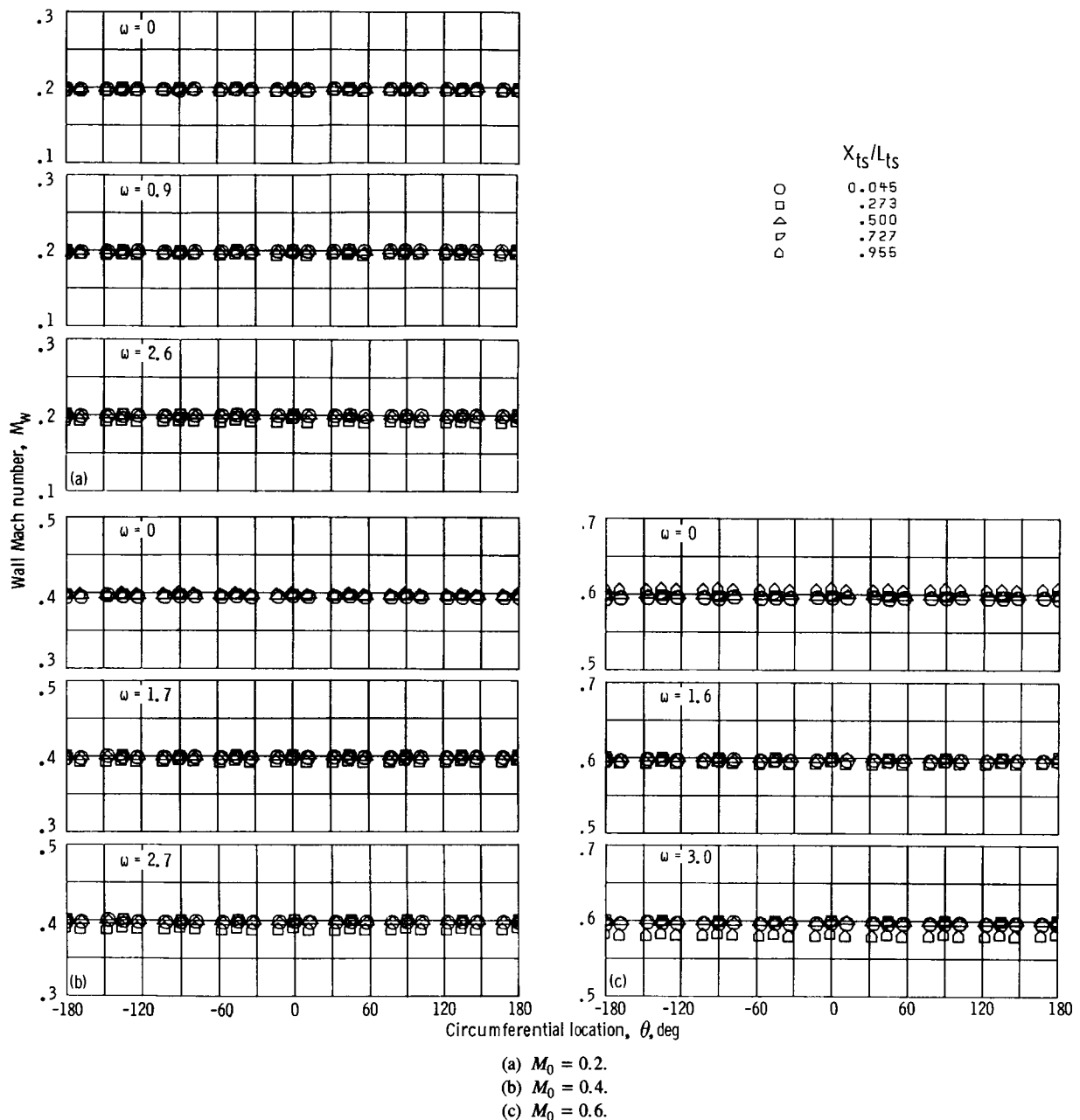
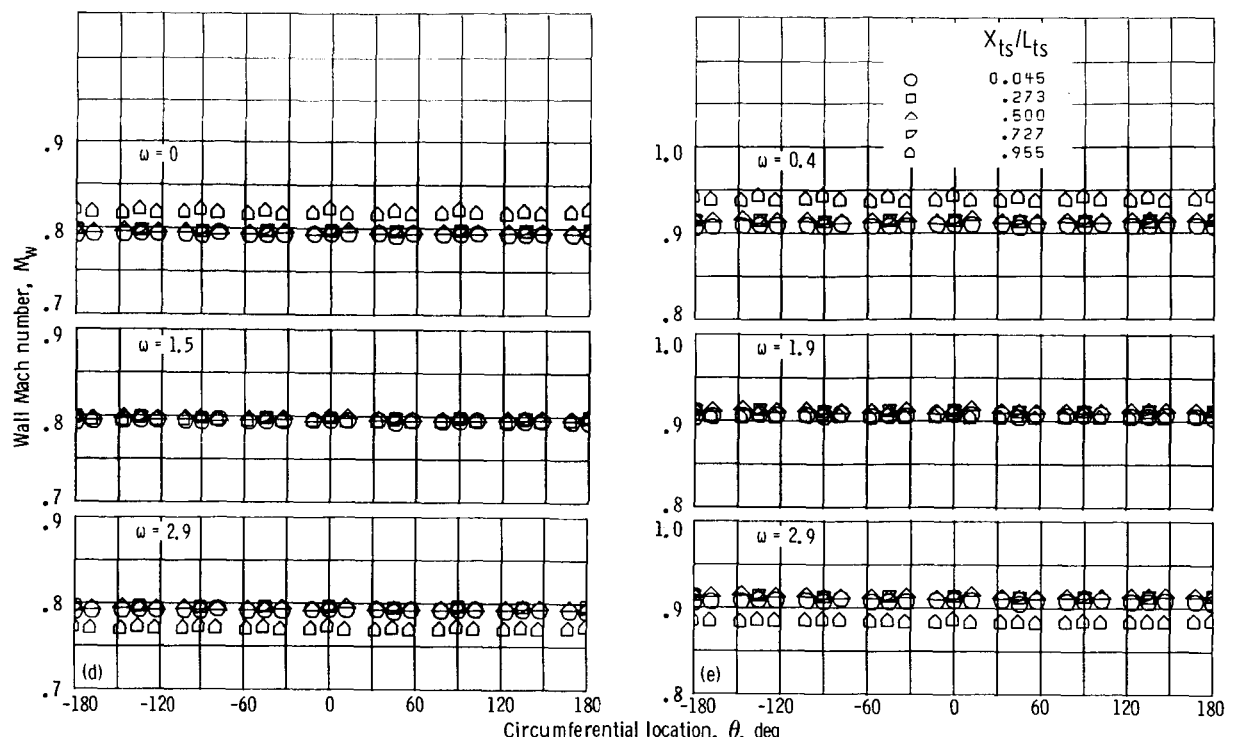


Figure 23.—Test-section wall circumferential Mach number distributions for flap angle of  $3^\circ$  and various PES flow rates  $\omega$ .



(d)  $M_0 = 0.8$ .  
 (e)  $M_0 = 0.92$ .

Figure 23.—Concluded.

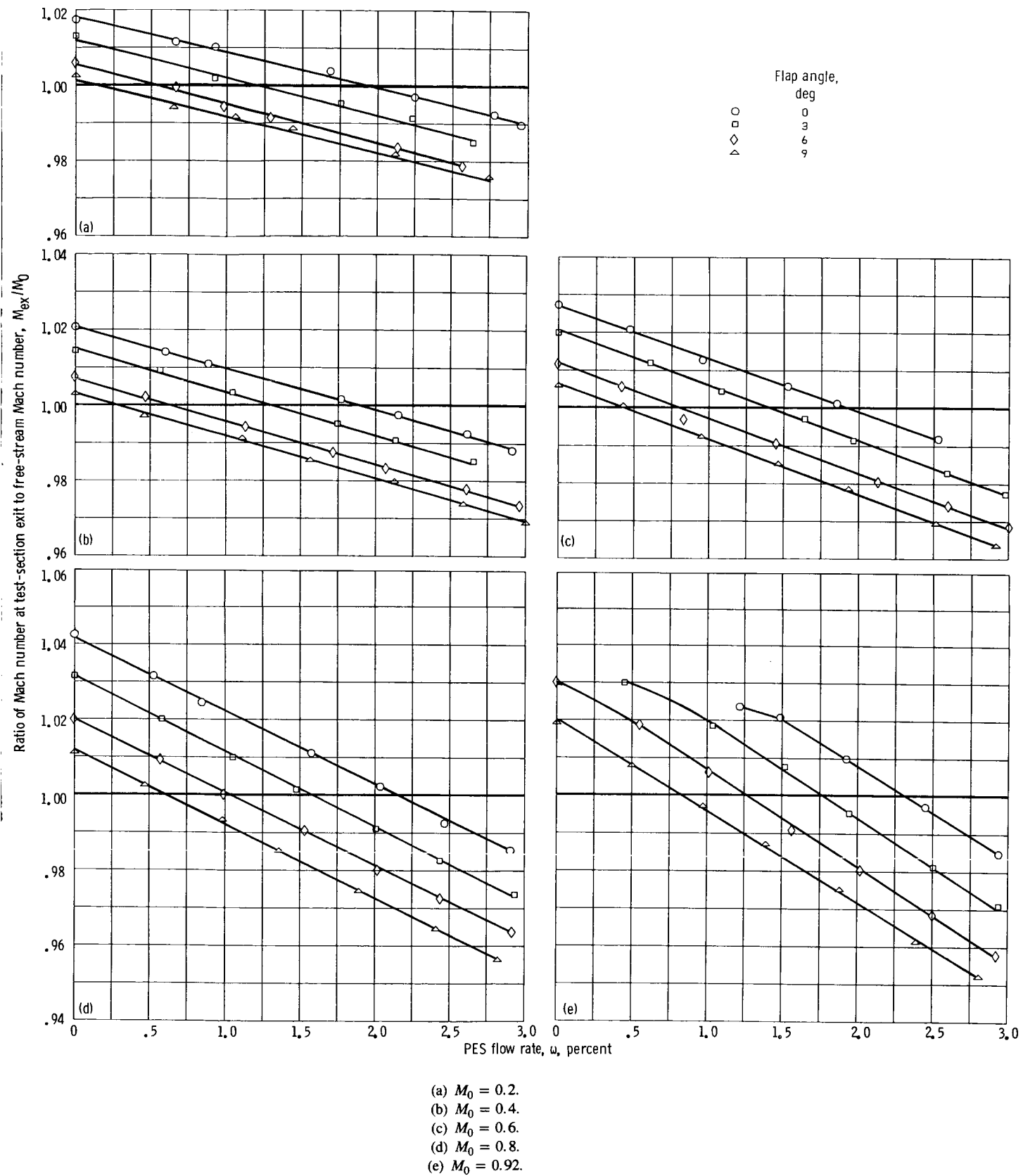


Figure 24.—Effect of PES flow rate on ratio of test-section exit Mach number to test-section free-stream Mach number  $M_{ex}/M_0$ .

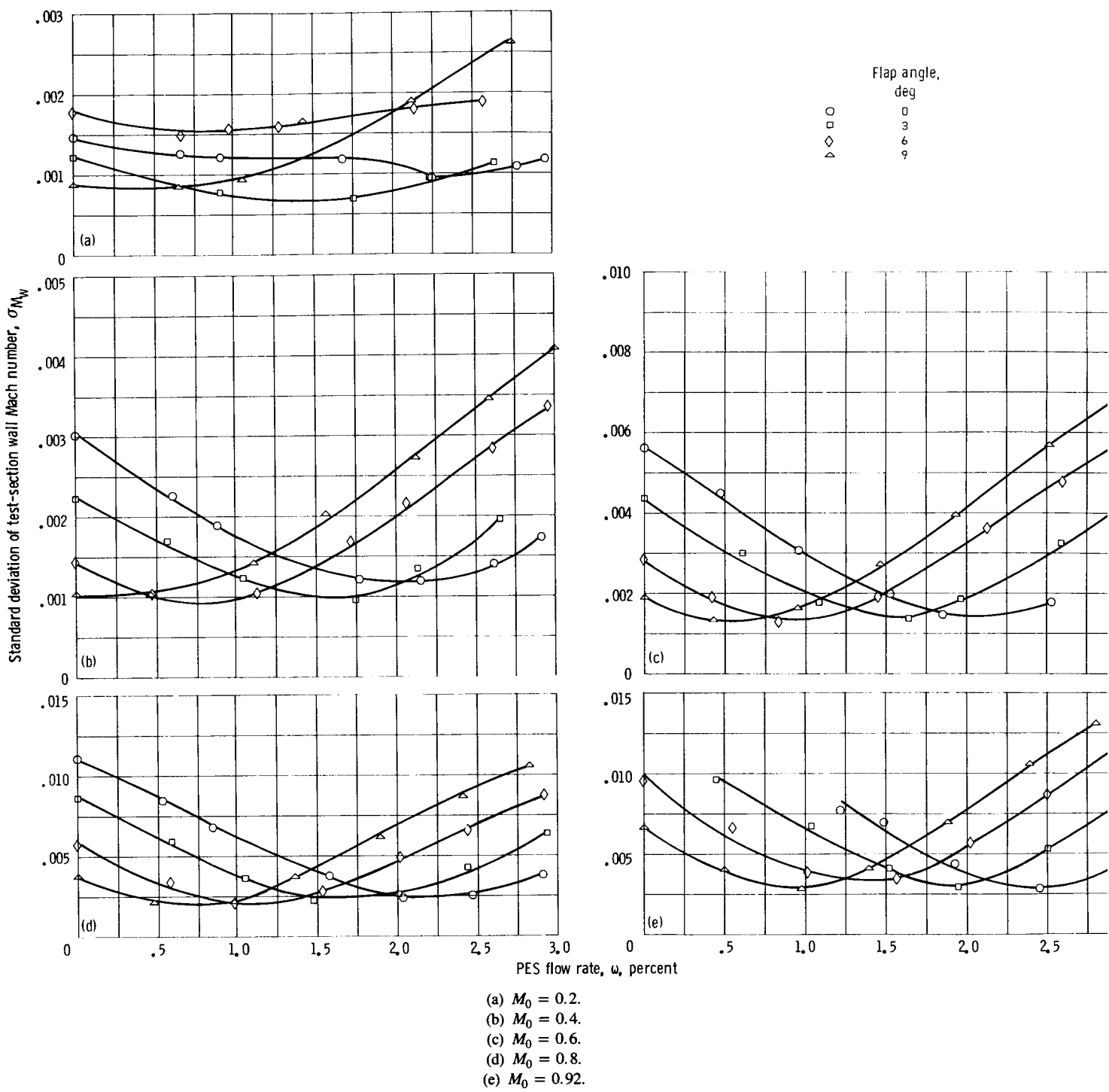


Figure 25.—Effect of PES flow rate on standard deviation of test-section wall Mach number  $\sigma_{M_w}$ .

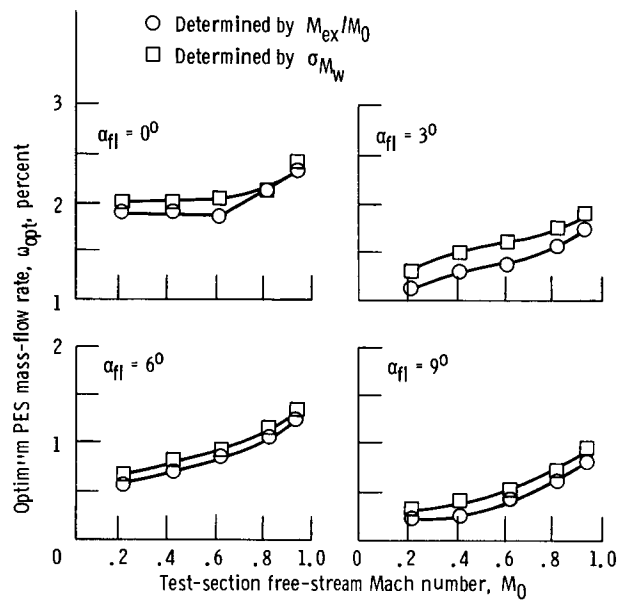


Figure 26.—Summary of optimum PES flow rates as determined by two different methods at flap angles of  $0^\circ$ ,  $3^\circ$ ,  $6^\circ$ , and  $9^\circ$ .

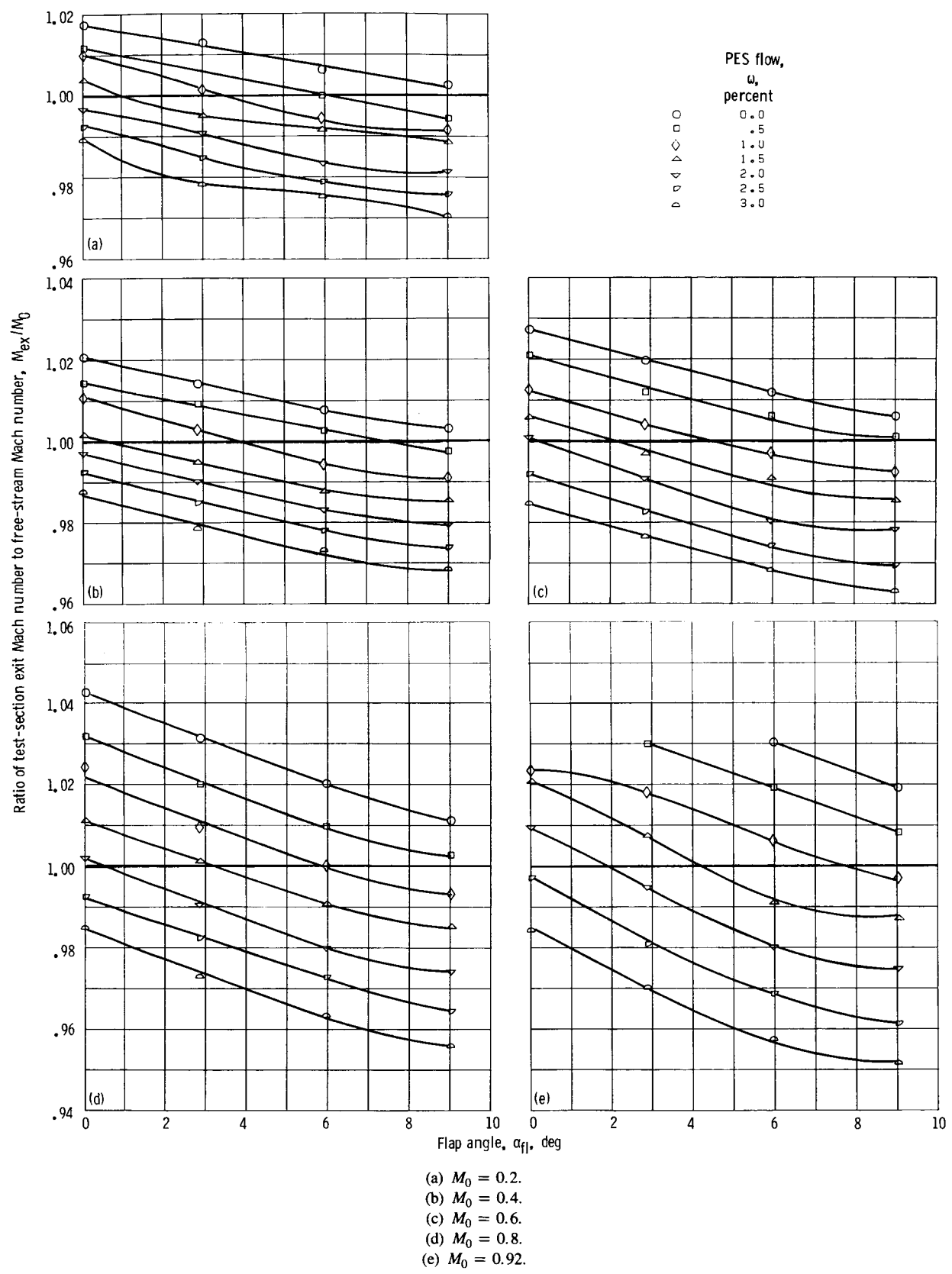


Figure 27.—Effect of flap angle on ratio of test-section exit Mach number to test-section free-stream Mach number  $M_{ex}/M_0$ .

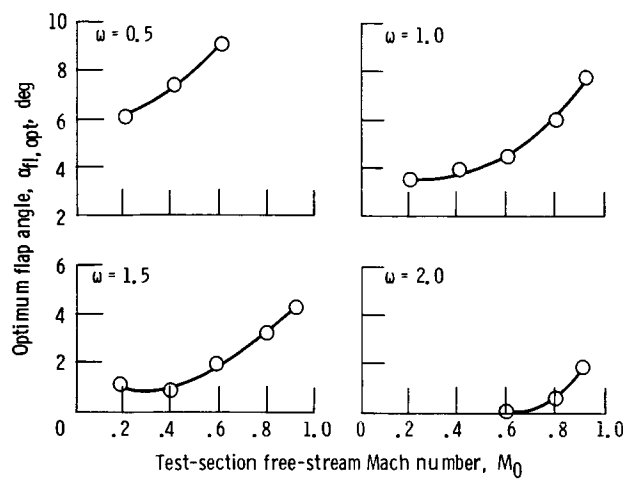


Figure 28.—Summary of optimum flap angles as determined by ratio of Mach number at test-section exit to the test-section free-stream Mach number ( $M_{ex}/M_0$ ) at various PES flow rates  $\omega$ .

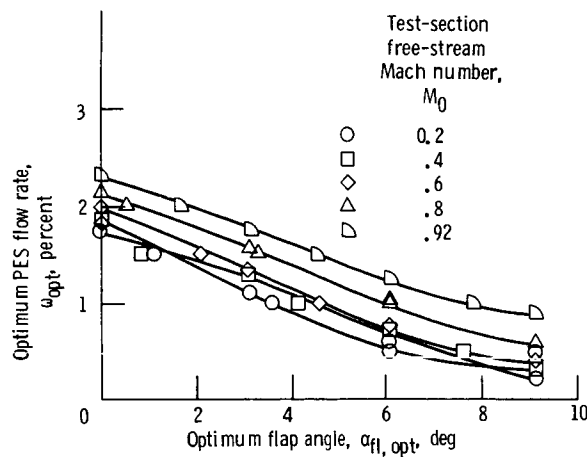
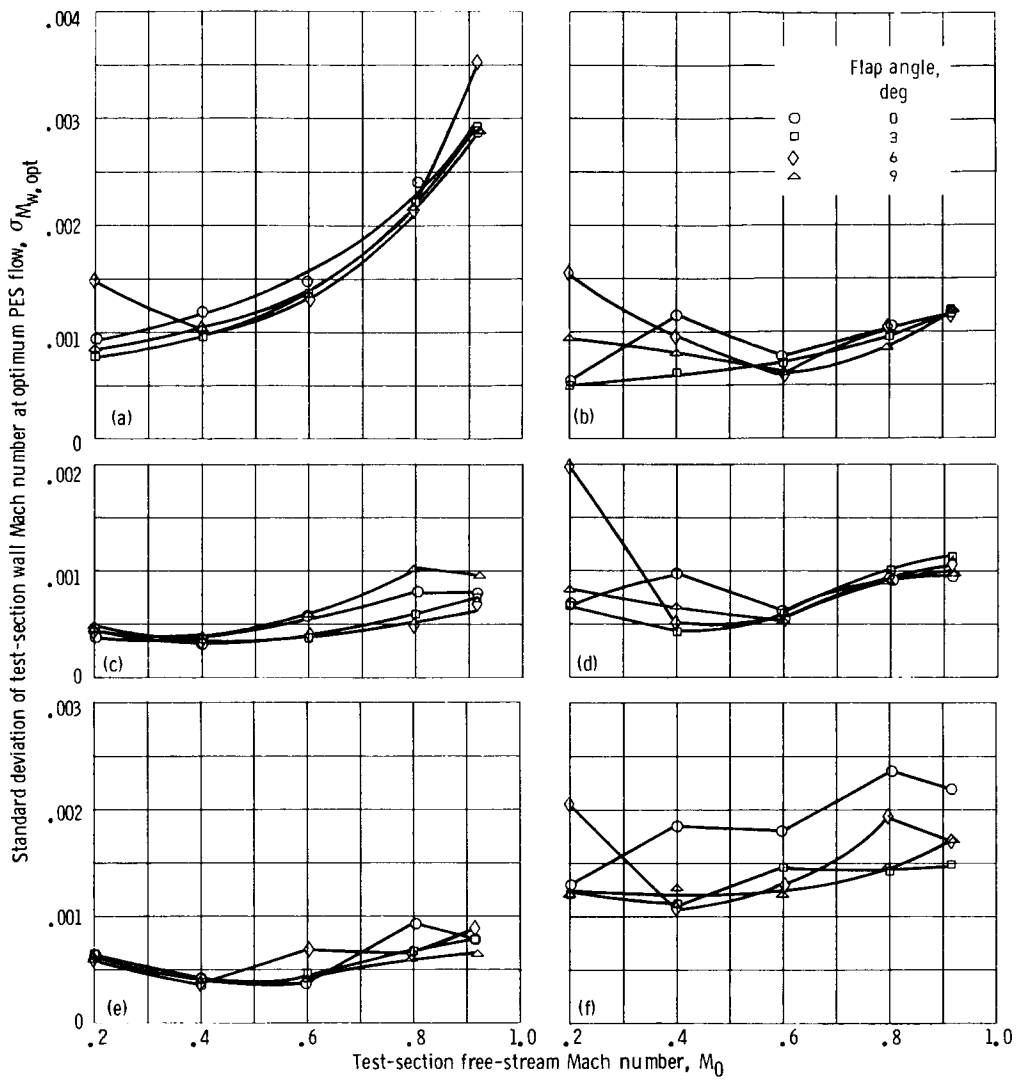
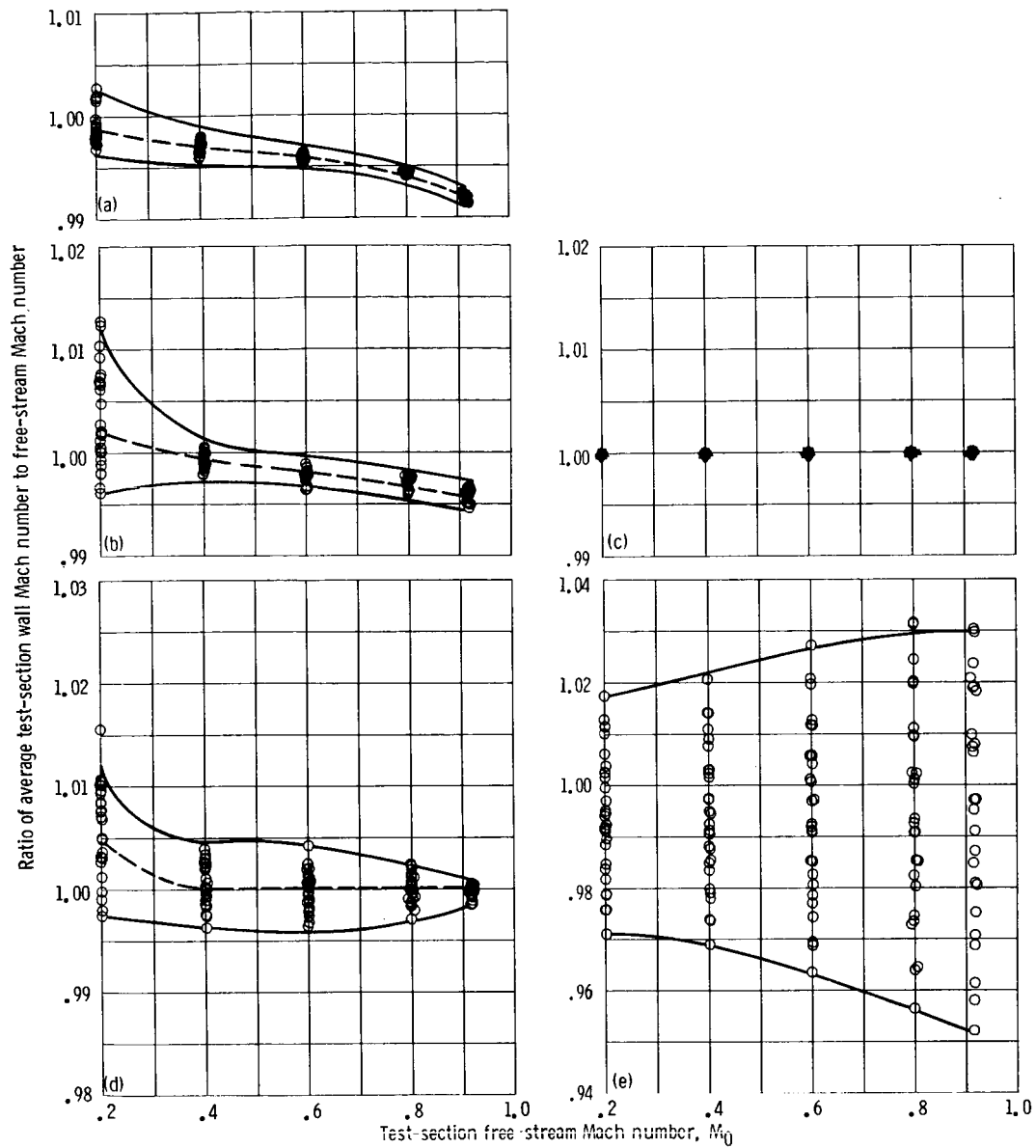


Figure 29.—Flap angle and PES flow tradeoff at optimum conditions.



- (a) Average test-section wall Mach number  $\bar{M}_w$
- (b) Mach number at nominal test-section entrance  $M_{en}; X_{ts}/L_{ts} = 0.045$ .
- (c) Mach number in forward portion of test section  $M_{for}; X_{ts}/L_{ts} = 0.273$ .
- (d) Mach number at midpoint of test section  $M_{mp}; X_{ts}/L_{ts} = 0.5$ .
- (e) Mach number in aft portion of test section  $M_{aft}; X_{ts}/L_{ts} = 0.727$ .
- (f) Mach number at nominal test-section exit  $M_{ex}; X_{ts}/L_{ts} = 0.955$ .

Figure 30.—Effect of test-section free-stream Mach number  $M_0$  on standard deviation of test-section wall Mach numbers  $M_w$  at optimum PES flow rates.



- (a) Mach number at nominal test-section entrance  $M_{en}; X_{ts}/L_{ts} = 0.045$ .
- (b) Mach number in forward portion of test section  $M_{for}; X_{ts}/L_{ts} = 0.273$ .
- (c) Mach number at midpoint of test-section  $M_{mp}; X_{ts}/L_{ts} = 0.50$ .
- (d) Mach number in aft portion of test section  $M_{aft}; X_{ts}/L_{ts} = 0.727$ .
- (e) Mach number at nominal test-section exit  $M_{ex}; X_{ts}/L_{ts} = 0.955$ .

Figure 31.—Ratio of average test-section wall Mach number  $M_w$  at various axial test-section locations to test-section free-stream Mach number  $M_0$ . Flap angles,  $0^\circ, 3^\circ, 6^\circ$ , and  $9^\circ$ ; PES flow rate, 0 to 3 percent.

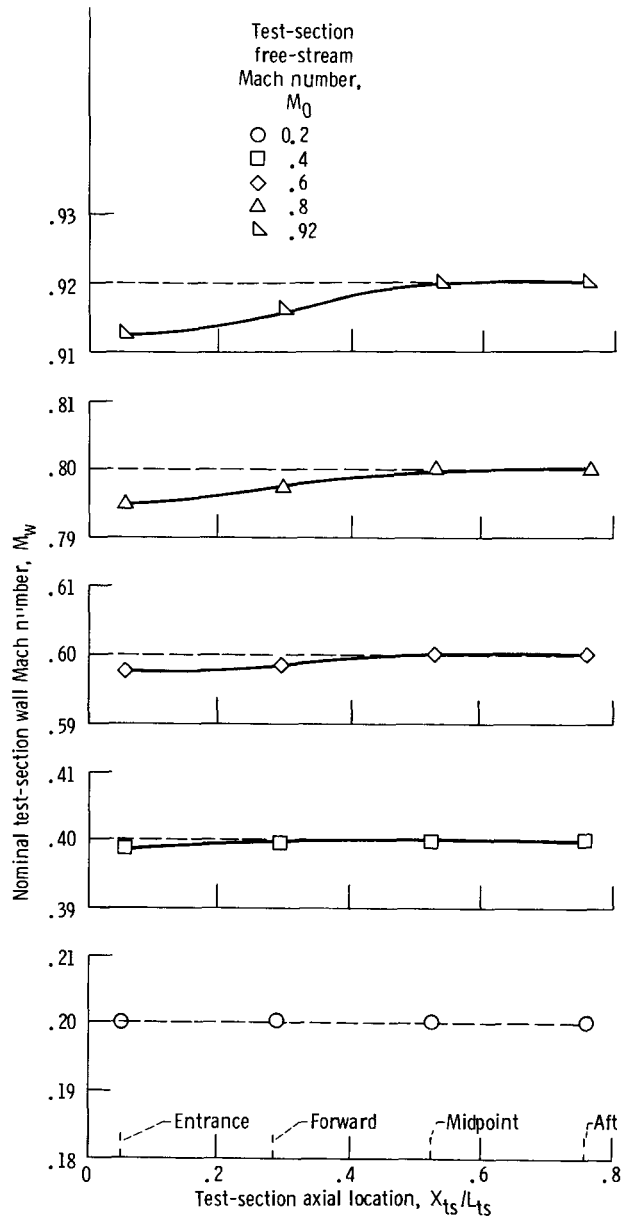


Figure 32.—Flow acceleration characteristics through test section. Flap angles,  $0^\circ$ ,  $3^\circ$ ,  $6^\circ$ , and  $9^\circ$ ; PES flow rates  $\omega$ , 0 to 3 percent.

|   |  |  |                   |
|---|--|--|-------------------|
| 1. Report No.<br>NASA TP-2666   | 2. Government Accession No.                          | 3. Recipient's Catalog No.   |                   |
| 4. Title and Subtitle<br><br>Experimental Evaluation of Wall Mach Number Distributions of the Octagonal Test Section Proposed for NASA Lewis Research Center's Altitude Wind Tunnel   |  | 5. Report Date<br>November 1986  |                   |
|   |  | 6. Performing Organization Code<br>505-62-3A                                 |                   |
| 7. Author(s)<br><br>Douglas E. Harrington, Richard R. Burley, and Robert R. Corban  |  | 8. Performing Organization Report No.<br>E-3145                              |                   |
|   |  | 10. Work Unit No.  |                   |
| 9. Performing Organization Name and Address<br><br>National Aeronautics and Space Administration<br>Lewis Research Center<br>Cleveland, Ohio 44135  |  | 11. Contract or Grant No.  |                   |
|   |  | 13. Type of Report and Period Covered<br>Technical Paper                     |                   |
| 12. Sponsoring Agency Name and Address<br><br>National Aeronautics and Space Administration<br>Washington, D.C. 20546   |  | 14. Sponsoring Agency Code   |                   |
| 15. Supplementary Notes   |  |  |                   |
| 16. Abstract<br><br>Wall Mach number distributions were determined over a range of test-section free-stream Mach numbers from 0.2 to 0.92. The test section was slotted and had a nominal porosity of 11 percent. Reentry flaps located at the test-section exit were varied from 0° (fully closed) to 9° (fully open). Flow was bled through the test-section slots by means of a plenum evacuation system (PES) and varied from 0 to 3 percent of tunnel flow. Variations in reentry flap angle or PES flow rate had little or no effect on the Mach number distributions in the first 70 percent of the test section. However, in the aft region of the test section, flap angle and PES flow rate had a major impact on the Mach number distributions. Optimum PES flow rates were nominally 2 to 2.5 percent with the flaps fully closed and less than 1 percent when the flaps were fully open. The standard deviation of the test-section wall Mach numbers at the optimum PES flow rates was 0.003 or less. |  |  |                   |
| 17. Key Words (Suggested by Author(s))<br><br>Wind tunnel; Test section; Subsonic; Slots;<br>Aerodynamics; Mach number; Flaps; Octagonal  |  | 18. Distribution Statement<br><br>Unclassified—unlimited<br>STAR Category 09 |                   |
| 19. Security Classif. (of this report)<br>Unclassified  | 20. Security Classif. (of this page)<br>Unclassified | 21. No of pages<br>36  | 22. Price*<br>A03 |

\*For sale by the National Technical Information Service, Springfield, Virginia 22161

NASA-Langley, 1986